Article

Structure

Structural Insights into Ca^{2+}-Calmodulin Regulation of Plectin 1a-Integrin β4 Interaction in Hemidesmosomes

Graphical Abstract

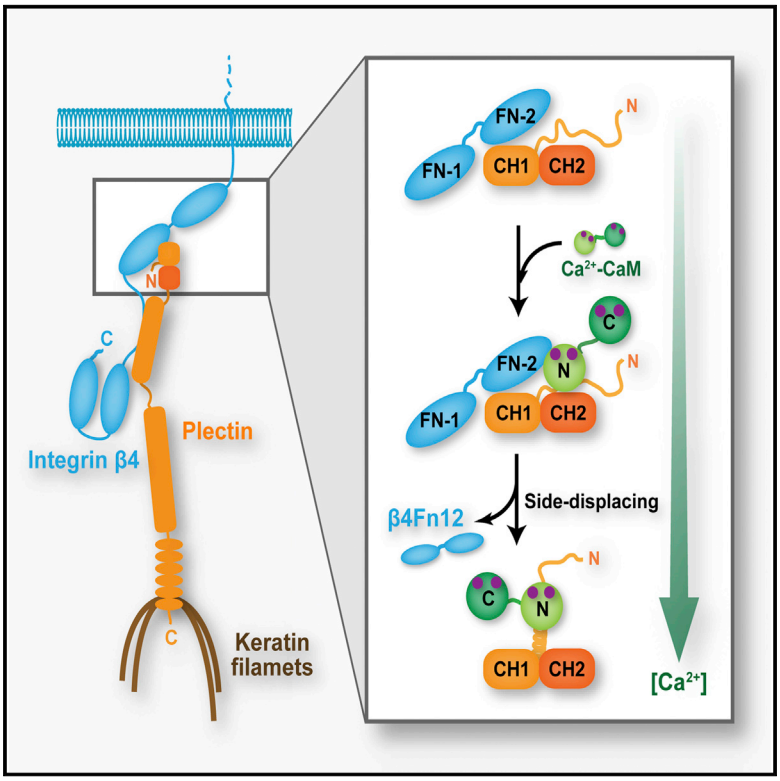

Authors

Jae-Geun Song, Julius Kostan, ..., Bettina Warscheid, Kristina Djinović-Carugo

Correspondence

kristina.djinovic@univie.ac.at

In Brief

Hemidesmosomes attach the top level of skin to plasma membrane via the assembly between integrin α6β4, plectin, and intermediate filaments. Hemidesmosome disassembly and remodeling are regulated by phosphorylation and Ca^{2+}. We provide a structural mechanism of how Ca^{2+}/CaM shunts integrin α6β4 and F-actin from the assembly with plectin.

Highlights

- Calmodulin binds to plectin 1a via its N-terminal lobe in an extended conformation
- The disordered N-ter tail of plectin 1a folds in an α helix upon calmodulin binding
- Suitably positioned calmodulin displaces integrin β4 from complex with plectin 1a

Accession Numbers

4Q59
4Q57
4Q58

Song et al., 2015, Structure *23*, 558–570
March 3, 2015
http://dx.doi.org/10.1016/j.str.2015.01.011

CellPress

Structure
Article

Structural Insights into Ca^{2+}-Calmodulin Regulation of Plectin 1a-Integrin β4 Interaction in Hemidesmosomes

Jae-Geun Song,[1,7] Julius Kostan,[1,7] Friedel Drepper,[2] Bettina Knapp,[2] Euripedes de Almeida Ribeiro, Jr.,[1] Petr V. Konarev,[3] Irina Grishkovskaya,[1] Gerhard Wiche,[4] Martin Gregor,[5] Dmitri I. Svergun,[3] Bettina Warscheid,[2] and Kristina Djinović-Carugo[1,6,*]

[1]Department of Structural and Computational Biology, Max F. Perutz Laboratories, University of Vienna, Vienna Biocenter (VBC), Campus Vienna Biocenter 5, A-1030 Vienna, Austria
[2]Department of Functional Proteomics and Biochemistry, Institute of Biology II and BIOSS Centre for Biological Signaling Studies, University of Freiburg, Schaenzlestrasse 1, D-79104 Freiburg, Germany
[3]EMBL-Hamburg c/o DESY, Notkestrasse 85, D-22603 Hamburg, Germany
[4]Department of Biochemistry and Cell Biology, Max F. Perutz Laboratories, University of Vienna, Dr. Bohrgasse 9, A-1030 Vienna, Austria
[5]Department of Integrative Biology, Institute of Molecular Genetics of the ASCR, Vídeňská 1083, Prague 4 CZ-14220, Czech Republic
[6]Department of Biochemistry, Faculty of Chemistry and Chemical Technology, University of Ljubljana, Aškerčeva 5, SI-1000 Ljubljana, Slovenia
[7]Co-first author
*Correspondence: kristina.djinovic@univie.ac.at
http://dx.doi.org/10.1016/j.str.2015.01.011

SUMMARY

The mechanical stability of epithelial cells, which protect organisms from harmful external factors, is maintained by hemidesmosomes via the interaction between plectin 1a (P1a) and integrin α6β4. Binding of calcium-calmodulin (Ca^{2+}-CaM) to P1a together with phosphorylation of integrin β4 disrupts this complex, resulting in disassembly of hemidesmosomes. We present structures of the P1a actin binding domain either in complex with the N-ter lobe of Ca^{2+}-CaM or with the first pair of integrin β4 fibronectin domains. Ca^{2+}-CaM binds to the N-ter isoform-specific tail of P1a in a unique manner, via its N-ter lobe in an extended conformation. Structural, cell biology, and biochemical studies suggest the following model: binding of Ca^{2+}-CaM to an intrinsically disordered N-ter segment of plectin converts it to an α helix, which repositions calmodulin to displace integrin β4 by steric repulsion. This model could serve as a blueprint for studies aimed at understanding how Ca^{2+}-CaM or EF-hand motifs regulate F-actin-based cytoskeleton.

INTRODUCTION

The skin forms a barrier against the environment and protects us from mechanical trauma, pathogens, radiation, dehydration, and perilous temperature fluctuations. It is composed of an epidermal and a dermal layer, which are separated by a basement membrane. The epithelium of the skin, the epidermis, is made primarily of keratinocytes, while the dermis contains different cell types, including fibroblasts, endothelial cells, and macrophages, as well as the extracellular matrix. Integrity of epithelial cells is maintained by multiprotein complexes termed hemidesmosomes (HDs), which attach the top level of the skin to plasma membrane (Green and Jones, 1996). HDs are dynamic structures, which can be quickly disassembled if required, for example, during wound healing, differentiation, or carcinoma invasion (Litjens et al., 2006). Integrin α6β4 is the principal player in the interaction between the intermediate filament (IF) cytoskeleton and extracellular matrix at the site of HDs, which traverses the plasma membrane (Borradori and Sonnenberg, 1999; Green and Jones, 1996). The cytoplasmic part of the β4 subunit is unusually long and consists of two pairs of fibronectin type III (FnIII) domains separated by the connecting segment (Tamura et al., 1990). On the cytoplasmic side, integrin α6β4 interacts with plectin, which mediates association between the HDs and the keratin cytoskeleton. Binding of plectin to the β4 subunit of integrin α6β4 is the critical step in the formation of HDs (Litjens et al., 2006). The importance of integrin α6β4 and plectin for stability of HDs is substantiated by in vivo studies in mice, which display reduced levels or complete absence of HDs when deficient in either plectin or integrin subunits α6 and β4 (Andra et al., 1997; Georges-Labouesse et al., 1996; van der Neut et al., 1996). In fact, inherited or acquired diseases in which integrin α6β4 or plectin are missing or are structurally perturbed result in tissue fragility and blistering (Walko et al., 2014).

Plectin, a member of the plakin family, connects different elements of the cytoskeleton and is expressed in a wide variety of mammalian cells (Castanon et al., 2013). At its N terminus there is an actin binding domain composed of two calponin homology (CH) domains, which is followed by a plakin domain, the coiled-coil rod of over 1,000 residues, six plectin repeat domains, and a short terminal tail. Due to alternative splicing, plectin is expressed as 11 isoforms with diverse N-ter sequences that dictate its differential subcellular targeting (Fuchs et al., 1999). Plectin 1a

(P1a) and 1c (P1c) are major isoforms of plectin expressed in basal keratinocytes. However, P1a is HD specific, while P1c colocalizes with microtubules (Andra et al., 2003; Walko et al., 2011).

Most of the efforts to understand the regulation of HD disassembly have focused on the main organizer of the HD, the α6β4 integrin. Multiple binding sites mediate the interactions between plectin and integrin α6β4, most of which are regulated by several phosphorylation events at the interaction interfaces (Frijns et al., 2010, 2012; Rabinovitz et al., 2004; Wilhelmsen et al., 2007). One site that is not regulated by phosphorylation is between the ABD of plectin and the first pair of the FnIII domains and the connecting segments of integrin β4 (Frijns et al., 2010; Geerts et al., 1999; Niessen et al., 1997; Rabinovitz et al., 2004; Wilhelmsen et al., 2007). Besides phosphorylation, Ca^{2+} also serves as a modulator in keratinocyte proliferation and differentiation. In particular, integrin α6β4 is downregulated during Ca^{2+}-induced differentiation of cultured keratinocytes (Kostan et al., 2009; Tennenbaum et al., 1996). Interestingly, Ca^{2+}/calmodulin (Ca^{2+}-CaM) was shown to reduce the interaction between integrin α6β4 and HD-specific P1a and to inhibit the interaction of P1a with F-actin in a Ca^{2+}-dependent manner (Kostan et al., 2009), thus contributing to the regulation of HD disassembly.

The aim of this study is to address the question of how Ca^{2+}-CaM regulates the P1a interaction with integrin β4 and F-actin, and whether the interaction mode with integrin β4 is isoform specific. Our results revealed the molecular mechanism underlying the Ca^{2+}-CaM regulation of the P1a/integrin β4 and P1a/F-actin interaction via shunting the integrin β4 and F-actin from the complex with P1a. Comparison with the structure of the complex between integrin β4 and the P1c isoform (de Pereda et al., 2009) shows that the plectin-integrin β4 interaction mode is not isoform specific, while Ca^{2+}-CaM binds to plectin in an isoform-specific manner. Based on these results, we suggested the model for Ca^{2+}-CaM-induced disruption of the P1aABD-integrin β4 complex. Finally, the related proteins α/β-spectrin, dystrophin, and utrophin (members of the spectrin superfamily), as well as F-actin binding protein filamin A, may be regulated in related ways by Ca^{2+}-CaM or by their own EF hands motifs.

RESULTS

Interaction of P1a and CaM in Epithelial Cells

Previous work has shown that Ca^{2+}-CaM interacts specifically with the ABD of isoform P1a (P1aABD) (Kostan et al., 2009). To further characterize the role of the N-ter isoform-specific sequence of P1a in binding to Ca^{2+}-CaM, we prepared several N-terminally truncated mutants of P1aABD. Pull-down assays were used in the presence of either Ca^{2+} or EDTA. While full-length P1aABD and mutant versions lacking the first 11 or 22 N-ter residues ($P1aABD_{\Delta11}$ and $P1aABD_{\Delta22}$) bound to CaM in a calcium-dependent manner, $P1aABD_{\Delta32}$ lacking 32 N-ter residues, and $P1aABD_{\Delta37}$ lacking the entire isoform-specific sequence failed to bind to Ca^{2+}-CaM (Figure S1). This suggested that interaction of Ca^{2+}-CaM with P1a is restricted to the N-ter region spanning residues 23–32.

To analyze CaM association with P1a in vivo, we performed Förster resonance energy transfer (FRET) analysis of the P1a-CaM interaction in 804G epithelial cells. The cells were cotransfected with cDNAs encoding C-terminally CFP-tagged P1aABD (P1aABD-CFP) or its mutant $P1aABD_{mut}$ ($P1aABD_{mut}$-CFP), and with C-terminally yellow fluorescence protein (YFP)-tagged CaM (CaM-YFP) (Figure 1A). The mutant $P1aABD_{mut}$ construct encoded two point mutations in the N-ter segment of P1a (Leu25Asp and Val29Asp) and was designed to be deficient in the interaction (see the section on "Crystal Structure of the P1a ABD in Complex with CaM N-ter Lobe"). The acceptor photobleaching method (Novotny et al., 2011) gave a positive FRET signal for the P1aABD-CFP/CaM-YFP pair (19% ± 0.9%). The $P1aABD_{mut}$-CFP fusion protein, however, showed a significantly lower FRET signal (6.2% ± 0.5%) despite a similar expression level, reaching the mean FRET efficiency of the P1aABD-CFP/empty YFP plasmid (8.0% ± 0.4%) used as a negative control (Figures 1A and 1B). These results confirmed that P1aABD interacts with CaM in vivo and that CaM binds to the isoform-specific N-ter segment of P1a.

P1a Interacts with the N-ter Lobe of CaM

In order to identify proximity residue pairs in the P1aABD/CaM complex, we applied chemical crosslinking combined with mass spectrometry (XL-MS) and bioinformatics analysis. We used the zero-length crosslinker 1-ethyl-3-(3-dimethylaminopropyl)carbodiimide (EDC) in the presence of *N*-hydroxysulfosuccinimide (sulfo-NHS). A band corresponding to ~50 kDa that appeared on SDS-PAGE upon one- or two-step crosslinking (Figure 2A) was excised, trypsinized, and analyzed by high-resolution liquid chromatography (LC)-MS/MS. In total, 12 crosslinks were identified for the P1aABD/CaM complex (Table S1). The major crosslinking products involve the adjacent K residues 36 and 37 at the border between the sequence-specific N-ter segment of P1aABD, and E14 residing in the A helix of the first CaM EF-hand. A representative MS/MS spectrum of a specific crosslinking product identifying a linkage between E14 of CaM and K37 of P1aABD is shown in Figure 2B. Other less prominent crosslinking products involve several sites of the C-lobe of CaM (CaM_{CL}). These data showed that both lobes of CaM have the capacity to interact with P1aABD. However, crosslinked peptides connecting the N-lobe of CaM (CaM_{NL}) to the N-ter tail of P1aABD were more prominent and more frequently detected (Table S1), suggesting a higher binding affinity of CaM_{NL}.

To quantify the preferential binding of CaM_{NL} to P1a, we determined and compared the binding affinities of CaM, CaM_{NL}, and CaM_{CL} with P1aABD by isothermal titration calorimetry (ITC). Schematic illustrations of plectin and CaM depicting the boundaries of the protein fragments used in this study are shown in Figure 3A. CaM binds to P1aABD more strongly (K_d 4.2 ± 0.4 μM) than CaM_{NL} alone (K_d 10.5 ± 1.1 μM), while CaM_{CL} displays even weaker affinity (K_d 27.7 ± 3.9 μM) (Figures 3B and 3C; Figure 7C), corroborating the XL-MS results. In a competitive experiment, CaM_{CL} was displaced when the P1aABD/CaM_{CL} complex was titrated with CaM_{NL} (Figure 3D). As expected, CaM_{CL} could not displace CaM_{NL} from the P1aABD/CaM_{NL} complex (Figure 3E). These results indicate that CaM_{NL} and CaM_{CL} bind to the same site on P1aABD, to which CaM_{NL} binds with higher affinity. Furthermore, full-length CaM has a higher affinity for P1aABD than CaM_{NL} alone, suggesting a possible auxiliary role of CaM_{CL} in the binding event. In summary, XL-MS data combined with ITC conclusively showed that CaM binds to P1a preferentially via its N-ter lobe.

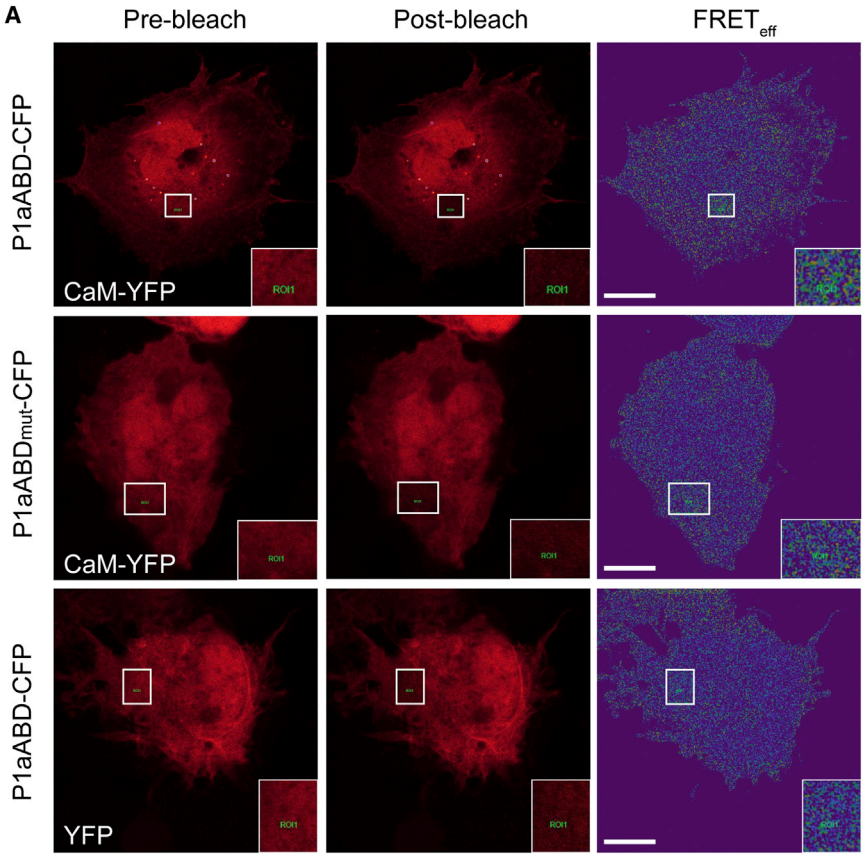

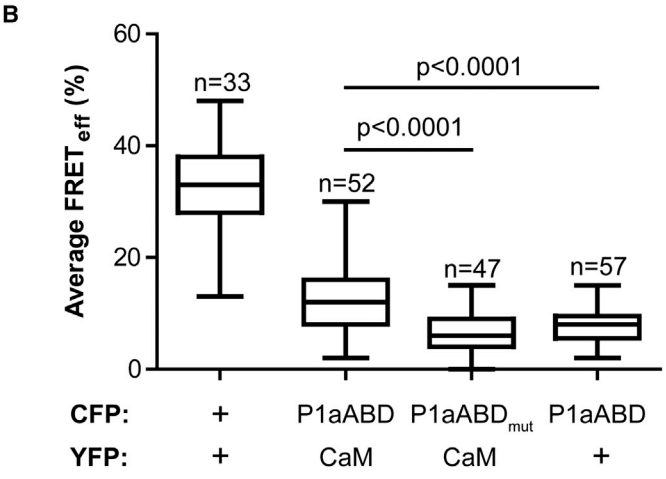

Figure 1. The P1aABD and CaM Interact In Vivo

(A) 804G cells ectopically expressing combinations of P1aABD-CFP and P1aABD$_{mut}$-CFP with CaM-YFP or YFP alone. FRET was measured by acceptor photobleaching. Pseudocolor pre- and postbleach images of acceptor (CaM-YFP or YFP alone) and FRET images (FRET$_{eff}$) are shown. FRET efficiency was determined as a relative increase of donor fluorescence in the cytoplasmic region of interest shown in boxed area, and enlarged in insets (bottom right corners). Bar, 10 μm.

(B) Box and whisker plots indicate the median FRET (middle line in the box), 25th percentile (bottom line of the box), 75th percentile (top line of the box), and minimum and maximum values (whiskers). A CFP-YFP fusion was used as a positive control for FRET (first column); cotransfection of P1aABD-CFP and empty YFP vector was used as a negative control (last column). The number of assessed cells/individual bleach events (n) obtained from three or more independent experiments is indicated.

Crystal Structure of the P1a ABD in Complex with CaM N-ter Lobe

To understand the structural basis of the Ca^{2+}-CaM–P1a interaction, we set out to determine the crystal structure. Prediction of disordered protein regions (Ishida and Kinoshita, 2007) suggested that the N-ter extension of P1a is intrinsically disordered (Figure S2) and hence its presence is unfavorable for crystallization studies. As we found the minimal region of P1a sufficient for the interaction with CaM to span N-ter residues 22–32, we first focused on crystallization of the P1aABD$_{\Delta22}$/CaM complex, which was unsuccessful. We therefore turned our attention to the P1aABD$_{\Delta22}$/CaM$_{NL}$ complex, since we showed that CaM$_{NL}$ binds to P1a with higher affinity than CaM$_{CL}$ (Figures 3B–3E). The structure of the P1aABD$_{\Delta22}$/CaM$_{NL}$ complex was determined to 1.8 Å resolution, with final R and R_{free} factors of 0.151 and 0.187, respectively. Data collection and refinement statistics are summarized in Table 1.

In the complex, CaM$_{NL}$ binds to the N-ter tail of P1a, which forms an α helix. This α helix extends the A helix of the first CH domain and protrudes away from the body of the ABD (Figure 4A). Each EF-hand of CaM$_{NL}$ coordinates one calcium ion (Figure 4A). Comparison of CaM$_{NL}$ with the crystal structure of unbound Ca^{2+}-CaM (Protein Data Bank [PDB], 3CLN) (Babu et al., 1988) (root-mean-square deviation (rmsd), 0.40 Å over 62 equivalent Cα atoms in N-lobe) showed that CaM$_{NL}$ did not change the conformation upon binding to plectin.

CaM$_{NL}$ binds to the N-ter extension of P1a mainly via hydrophobic interactions. Three hydrophobic residues of P1aABD$_{\Delta22}$ (L25, V29, and A32) are buried in the hydrophobic cleft of CaM$_{NL}$ (Figure 4B), consistent with the known binding motif of Ca^{2+}-CaM, termed 1-5-8, which bears hydrophobic residues at these positions (Rhoads and Friedberg, 1997). To assess the role of these residues in binding to Ca^{2+}-CaM, we mutated amino acids at motif positions 1 and 5 to negatively charged residues (L25D and V29D; P1aABD$_{mut}$). We showed by ITC, size exclusion chromatography (SEC), and FRET analysis that the P1aABD$_{mut}$ does

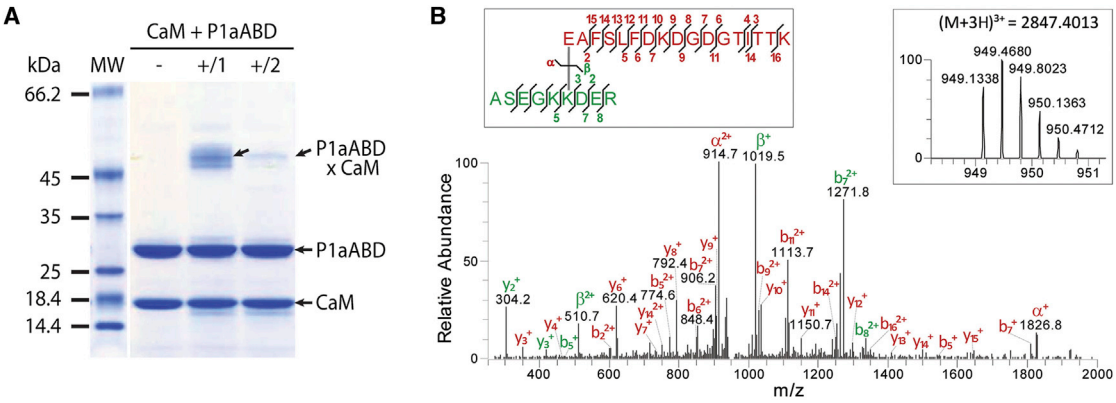

Figure 2. P1aABD Associates Preferentially with the N-ter Lobe of CaM

(A) SDS-PAGE analysis of the P1aABD/CaM complex crosslinked by EDC and sulfo-NHS. Proteins were incubated in the binding buffer either in the absence of crosslinker (-), or subjected to EDC and sulfo-NHS in a one-step (+/1) or two-step (+/2) reaction (for details see Supplemental Materials and Methods). Complexes of crosslinked P1aABD and CaM are readily visible as a higher-molecular weight band (arrow).

(B) MS/MS spectrum identifying a pair of crosslinked peptides after in-gel proteolysis of the complex band obtained by two-step crosslinking of CaM and P1aABD. Fragment ions are annotated for the α-peptide (red) and the β-peptide (green). Insets show mapping of the fragment ions onto the crosslinked peptide sequences (left) and the corresponding high-resolution MS spectrum displaying the isotopic distribution of the crosslinking product (right).

see also Table S1.

not interact with Ca^{2+}-CaM, confirming that the hydrophobic positions 25 and 29 are essential for binding (Figure 1; Figure S3).

Two polar contacts further stabilize the complex: an interaction between Q41 (in the loop between helices B and C of CaM_{NL}) and R31 of P1a (in the N-ter tail), and a salt bridge between E14 (in the A helix of EF-hand 1) and R40 in P1a (in the A helix of the CH1 domain). The latter seems less important for CaM binding, as other plectin isoforms that do not bind to Ca^{2+}-CaM also host an R at this position (Figure 4C). Finally, mapping the crosslinked residues on the three-dimensional structure of the $P1aABD_{\Delta22}/CaM_{NL}$ complex showed that the carboxylate group of E14 in CaM_{NL} is 5.7 Å and 7.0 Å away from the amino groups of plectin residues K36 and K37 (Figure 4C), respectively, which is in good agreement with the XL-MS results (Figure 2B; Table S1).

CaM Binds to P1a in an Extended Conformation

To determine the low-resolution shape of the nontruncated P1aABD in complex with full-length Ca^{2+}-CaM, small-angle X-ray scattering (SAXS) experiments were conducted (Table S2). The R_g of Ca^{2+}-CaM in the complex with P1aABD (20.9 Å; CRYSOL [Svergun et al., 1995]) was found to be similar to the R_g of extended Ca^{2+}-CaM in solution (21.3 ± 0.2 Å) (Heidorn and Trewhella, 1988). This indicated that the Ca^{2+}-CaM in complex with P1aABD exhibits an extended conformation in which the two lobes are connected with an interlobe linker, modeled here with dummy residues (Figures 4D and 4E). Furthermore, in the P1aABD/CaM complex, neither the CaM_{CL} nor the first 22 residues of the N-ter tail of P1a participate in the interaction.

The CaM binding motif of P1aABD (L25-V29-A32) represents a subgroup of 1-5-8-14 motifs in which hydrophobic residues at position 1 and 14 are the primary requirements for Ca^{2+}-CaM binding and anchoring the interaction partner to the two lobes of CaM (Figure S2) (Rhoads and Friedberg, 1997). P1a contains D38 at position 14, suggesting that the C-terminal lobe of CaM cannot bind due to the absence of a hydrophobic residue at this site. In addition, D38 is the first residue of helix A of the CH1 domain, and binding of the C-terminal lobe to this site would lead to a steric clash of helix C of CaM with the ABD, as shown by superposition of CaM_{NL} in complex with $P1aABD_{\Delta22}$ on Ca^{2+}-CaM in complex with skeletal muscle light chain kinase (PDB, 1CDL) (Chattopadhyaya et al., 1992) (rmsd, 0.684 Å over 57 Cα) (Figure S4). In summary, our results showed that Ca^{2+}-CaM binds with CaM_{NL} to a 1-5-8-type recognition site on the P1aABD N-ter tail in an extended conformation. This is to our best knowledge the first example of a complex in which Ca^{2+}-CaM binds to the interaction partner via its N-ter lobe in an extended conformation. Namely, a search of PDB for complexes in which CaM binds to the interaction partner in extended conformation gave seven hits, but in all of them, only the C-ter lobe or both lobes are involved in binding (Table S3).

N-ter Tail of P1a Folds upon Binding to CaM

Although the N-ter segment of P1aABD is predicted to be intrinsically disordered (Figure S2B), the amino acid residues 23–37 form an α helix in the $P1aABD_{\Delta22}/CaM_{NL}$ complex (Figures 4A and 4B), a feature often observed by intrinsically disordered proteins (Dyson and Wright, 2005). To validate the bioinformatics prediction that the entire N-ter tail is structurally disordered in the absence of Ca^{2+}-CaM, we solved the crystal structure of $P1aABD_{\Delta22}$ and performed SAXS analysis of P1ABD.

The electron density of the first 15 residues (aa 23–37) preceding the CH1 domain was missing in the crystal structure of $P1aABD_{\Delta22}$ (Figure 5A; Table 1), suggesting that this part of the protein is structurally disordered. SDS-PAGE analysis of the crystals confirmed that the N-ter tail was intact and was not proteolytically removed in the process of crystallization. In addition, no significant conformational changes took place in the ABD upon Ca^{2+}-CaM binding, as shown by comparison of $P1aABD_{\Delta22}$ in complex with CaM_{NL} with the structure of

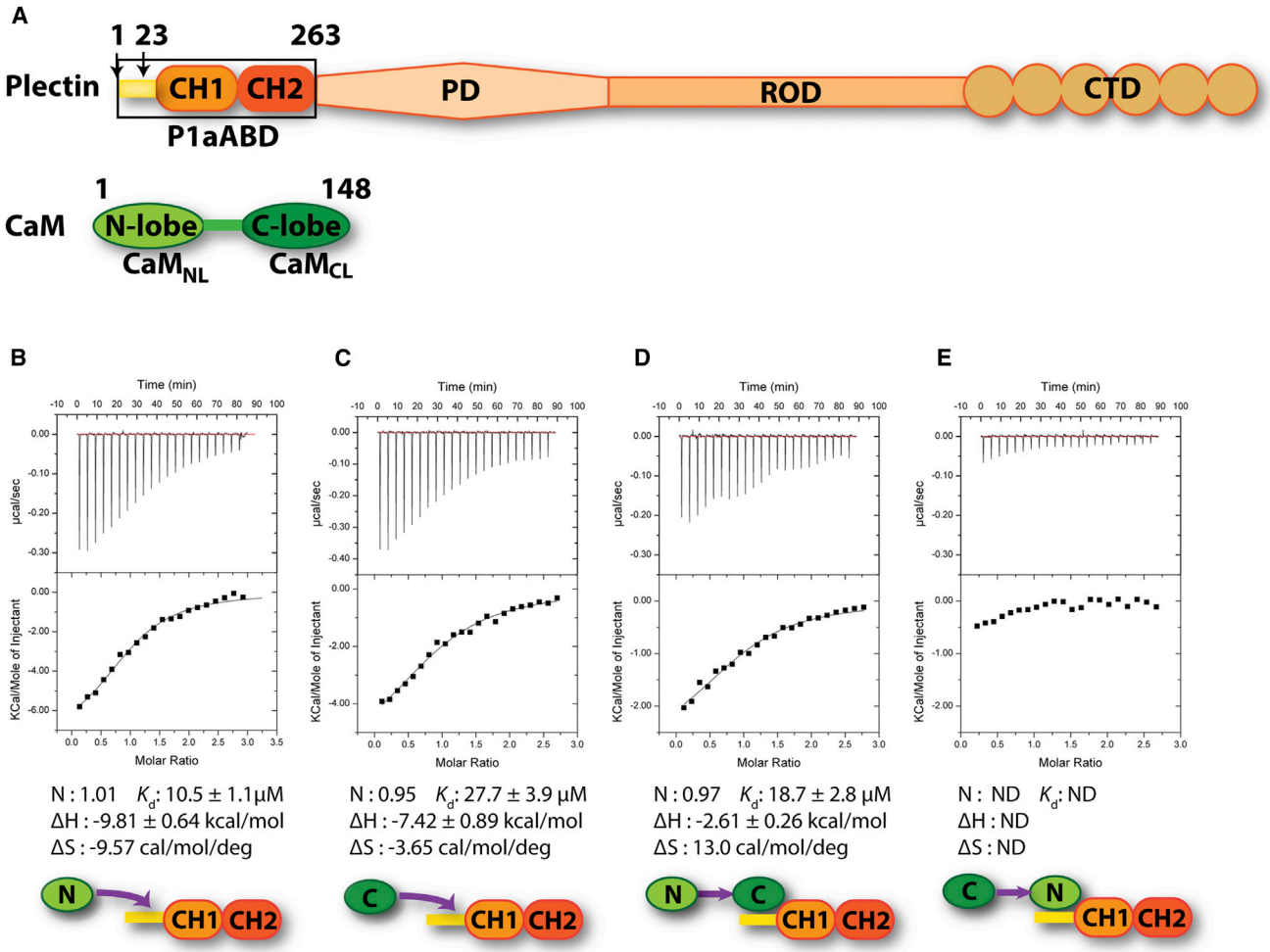

Figure 3. N-ter Lobe of CaM Binds to P1aABD with Higher Affinity Than the C-ter Lobe

(A) Schematic illustrations of plectin and CaM. CH, calponin homology domain; PD, plakin domain; ROD, coiled-coil rod domain; CTD, C-terminal domain. Arrows indicate positions of the first N-ter residue of P1aABD and P1aABD$_{\Delta 22}$ constructs, respectively. Schematic illustration of the P1a fragment used in the assays is shown in boxed area.

(B–E) ITC assays showing preferential binding of CaM$_{NL}$ to P1aABD. (B) P1aABD (40 µM) was titrated with CaM$_{NL}$ (400 µM). (C) P1aABD (40 µM) was titrated with CaM$_{CL}$ (400 µM). (D) P1aABD/CaM$_{CL}$ complex (40/60 µM) was titrated with CaM$_{NL}$ (400 µM). (E) P1aABD/CaM$_{NL}$ complex (40/60 µM) was titrated with CaM$_{CL}$ (400 µM). Data are expressed as mean values ± SD. ND, not determined.

P1aABD$_{\Delta 22}$ alone (Figure S5) (rmsd, 0.69 Å over 209 equivalent Cα atoms).

In the SAXS analysis of P1ABD, the N-ter extension was modeled as an ensemble of structurally variable moieties using the Ensemble optimization method (EOM) (Bernado et al., 2007), while the crystal structure of P1aABD$_{\Delta 22}$ was used as a rigid-body constraint. This yielded a fit to the experimental data with χ = 1.09 (Figure 5B, inset). Data collection and structural parameters derived from SAXS analysis on P1aABD are reported in Table S2. EOM analysis showed a broad R_g distribution, typical of extended and flexible structures (Figure 5B). Eight models from the selected ensemble (50 models) superimposed on ABD show that the N-ter tails of plectin isoform 1a adopt extended and variable conformations (Figure 5C). These data show that the N-ter segment of P1a is structurally disordered in the unbound state; however, it folds into an α helix upon binding to Ca^{2+}-CaM, undergoing a coupled folding and binding process (Dyson and Wright, 2005).

N-ter Tail of P1a Is Not Involved in Interaction with Integrin β4

Our structural and biochemical data showed that Ca^{2+}-CaM interacts with the N-ter isoform-specific sequence of P1a via its N-ter lobe. In vivo, this interaction contributes to the disassembly of the P1a-integrin β4 complex. In the published structure of the P1cABD/integrin β4 complex, the N-ter tail of P1c binds to integrin β4 mainly through the polypeptide backbone (de Pereda et al., 2009). In order to address the question whether this interaction mode is isoform specific and whether the coupled folding and binding mechanism observed for the interaction with Ca^{2+}-CaM applies also for the interaction of P1a and integrin β4, we determined the crystal structure of P1aABD in complex with the first pair of the FnIII domains of integrin β4. A construct

Table 1. Data Collection and Refinement Statistics

	P1aABD$_{\Delta22}$/CaM$_{NL}$	P1aABD$_{\Delta22}$/β4Fn12	P1aABD$_{\Delta22}$
Data Collection			
Source	ID14-1 (ESRF)	ID23-2 (ESRF)	ID14-4 (ESRF)
Wavelength (Å)	0.933	0.873	0.939
Resolution (Å)	48.93–1.8 (1.9–1.8)[a]	48.16–4.0 (4.47–4.0)	60.37–2.30 (2.38–2.30)
Space group	$P2_12_12_1$	$P6_5$	$C222_1$
Unit cell (Å, °)	a = 59.08, b = 65.38, c = 87.3 α = β = γ = 90	a = 96.32, b = 96.32, c = 207.8 α = 90, β = 90, γ = 120	a = 41.60, b = 159.39, c = 183.83 α = 90, β = 90, γ = 90
Molecules/a.u.	2	4	2
Unique reflections	31805 (4301)	9188 (2594)	28020 (2698)
Completeness (%)	99.2 (94.7)	99.1 (99.5)	99.7 (99.8)
R_{merge}[b]	0.095 (0.488)	0.272 (0.793)	0.125 (0.424)
R_{meas}[c]	0.101 (0.527)	0.300 (0.879)	0.143 (0.483)
R_{pim}[d]	0.033 (0.193)	0.123 (0.364)	0.067 (0.224)
Multiplicity	9.4 (7.2)	5.7 (5.6)	4.4 (4.2)
Mean *I*/sig(*I*)	17.5 (3.7)	7.4 (3.9)	6.9 (2.2)
CC (1/2)[e]	0.998 (0.877)	0.977(0.751)	0.945 (0.856)
Refinement			
R_{work}[f]/R_{free}[g]	0.151/0.187	0.224/0.287	0.183/0.245
Rmsd bonds (Å)	0.007	0.004	0.009
Rmsd angles (°)	0.963	0.892	1.246
Ramachandran outliers	0	0	0

see also Figure S5.

[a]Values in parentheses are for the highest-resolution shell.

[b]$R_{merge} = \sum|I_i - \langle I_i\rangle| / \sum I_i$, where I_i is the intensity of the *i*th observation, and $\langle I_i\rangle$ is the mean intensity of the reflection.

[c]$R_{meas} = \sum_{hkl}[N/(N-1)]^{1/2}\sum_i|I_i(hkl) - \langle I(hkl)\rangle| / \sum_{hkl}\sum_i I_i(hkl)$.

[d]$R_{pim} = \sum_{hkl}[1/(N-1)]^{1/2}\sum_i|I_i(hkl) - \langle I(hkl)\rangle| / \sum_{hkl}\sum_i I_i(hkl)$, where $I_i(hkl)$ is the observed intensity, and $\langle I(hkl)\rangle$ is the average intensity of multiple observations of symmetry-related reflections.

[e]CC(1/2) = the Pearson correlation coefficient of random half data sets.

[f]$R_{work} = \sum_{hkl}||F_o| - |F_c|| / \sum_{hkl}|F_o|$, calculated from working data set.

[g]R_{free} is calculated from 5% of data randomly chosen and not included in refinement.

encompassing the first two FnIII domains of integrin β4 (β4Fn12; 1126–1355) was used for crystallization with P1aABD$_{\Delta22}$ (Figure 6A). The asymmetric unit contained one P1aABD$_{\Delta22}$/β4Fn12 complex and one free copy of ABD and β4Fn12 each. The structure was determined to 4.0 Å resolution and refined to the final R_{work} and R_{free} factors of 0.224 and 0.287, respectively (Figure 6B; Table 1).

Structural comparison of our P1aABD$_{\Delta22}$/β4Fn12 complex with the complex of P1cABD/β4Fn12 (PDB, 3F7P; de Pereda et al., 2009) showed that no substantial conformational differences occurred and that the overall architecture was maintained in both complexes (rmsd, 0.87 Å over 367 equivalent Cα atoms). The first 15 residues of the P1aABD$_{\Delta22}$ construct were not visible in the electron density of the P1aABD$_{\Delta22}$/β4Fn12 crystal structure, suggesting that it is structurally disordered in this complex and most likely not involved in the interaction with integrin β4. This was further confirmed by data showing that the P1a N-ter segment encompassing residues (1–60 aa) does not bind to β4Fn12 in ITC assays (Figure S6A).

To further characterize and validate the architecture of the P1aABD/β4Fn12 complex in solution, we performed SAXS analysis. Data collection and structural parameters are summarized in Table S2. The ab initio molecular envelope yielded a fit of $\chi^2 = 1.01$ (Figure S7A) and agreed well with the crystal structure (Figure S7B). Since the concentration of the sample used (41.3 μM) was similar to the K_d (41.7 μM) of the complex determined by ITC (Figure 7B), a polydisperse solution (calculated 38.0% of complex) was expected. To account for this, we used the program OLIGOMER (Konarev et al., 2003) to determine the volume fractions of the complex and its subunits in solution. The best fit to the experimental data (χ^2 = 0.90) corresponded to a mixture containing 54% ± 3% of the complex, 25% ± 3% of P1aABD, and 21% ± 3% of β4Fn12, in line with the K_d-based estimation. To further validate the structures of the P1aABD/β4Fn12 complex, we used XL-MS. Mapping the crosslinked residues on the three-dimensional structure of the complex further corroborated the structural results (Figures S8A and S8B): four crosslinked peptides cluster to one site in the P1aABD/β4Fn12 complex (Table S1). Both plectin K36 and K37, located on the border between helix A of the CH1 domain and the N-terminal segment, were crosslinked to integrin β4 residue E1286 residing on the loop between two β strands in the FnIII-2 domain. These lysine residues of plectin are in contact with CaM in the P1aABD$_{\Delta22}$/CaM$_{NL}$ complex (Figure 2B; Figure 4C), indicating that interaction with CaM should exclude that with integrin β4. In the crystal

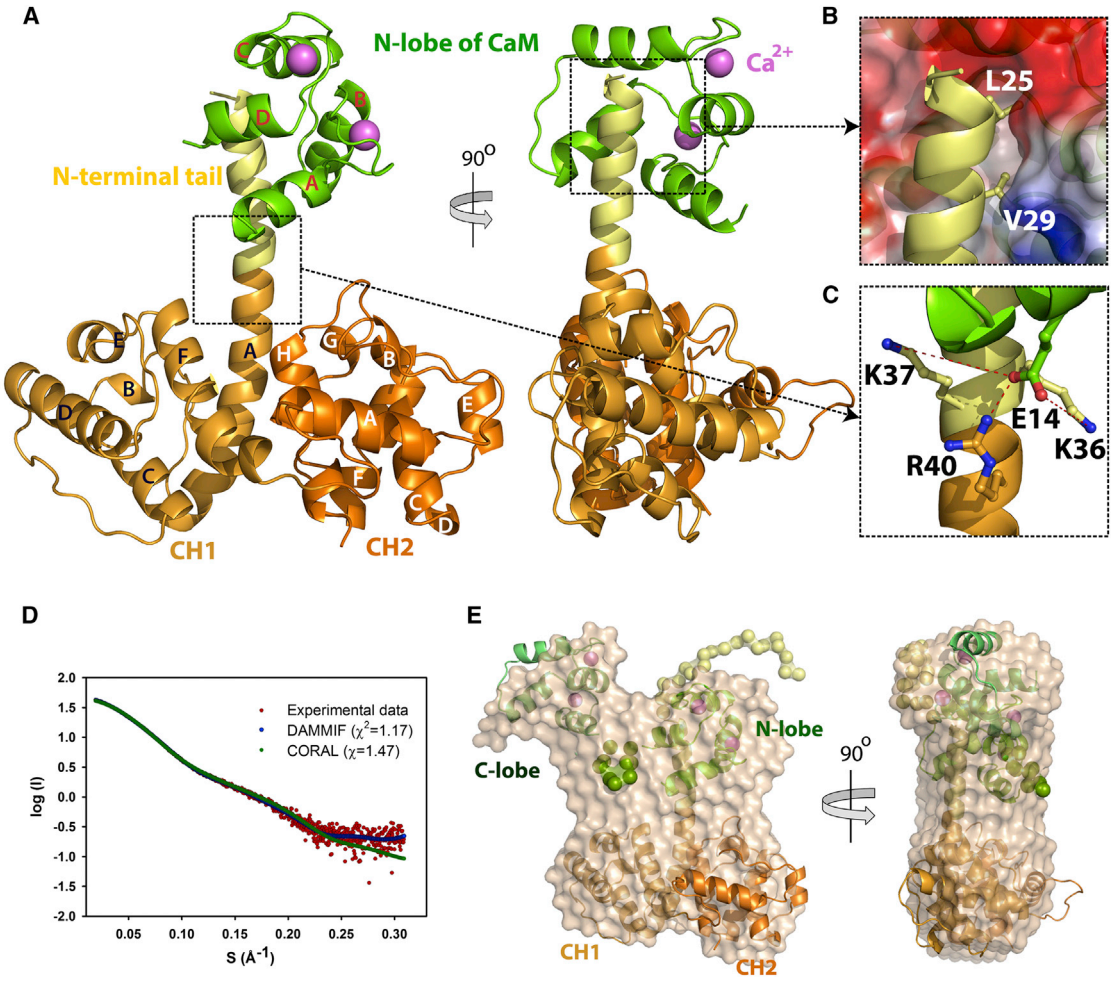

Figure 4. Structure of the P1aABD/CaM Complex

(A) Crystal structure of the P1aABD$_{\Delta 22}$/CaM$_{NL}$ complex. The complex is displayed in two orientations (90° rotated along the *y* axis). CH1 and CH2 in the ABD are colored respectively in bronze and orange, the N-ter tail of P1a in yellow and CaM$_{NL}$ in green. Ca^{2+} is depicted as a violet sphere.

(B) The binding interface of the P1aABD$_{\Delta 22}$/CaM$_{NL}$ complex. CaM$_{NL}$ is shown according to electrostatic surface potential, with blue and red depicting positive and negative electrostatic potentials, respectively. Two residues of P1a (L25 and V29) important for interaction with CaM are buried in the hydrophobic cleft of CaM$_{NL}$.

(C) A salt bridge between E14 of CaM and R40 of plectin (2.7 Å apart). XL-MS analysis shows that CaM E14 is crosslinked with K36 (5.7 Å apart) and K37 of plectin (7.0 Å).

(D) Experimental SAXS data of the P1aABD/CaM complex is shown in red; calculated scattering curves from SAXS models are individually presented in green (rigid-body modeling by CORAL) and blue (ab initio modeling by DAMMIF) lines.

(E) The ab initio molecular shape of the P1aABD/CaM complex (shown in transparent beads) was superimposed over the SAXS-derived rigid-body model of the complex. Flexible residues (1–21 residues of P1aABD and 74–82 residues of CaM) were modeled as dummy residues (colored spheres).

see also Figure S4; Table S2.

structure, the first residue of the CH1 domain visible in the electron density is D38, located 12.8 Å from integrin β4 Glu1286 (Cα–Cα distance, Figure S8C), showing that the two adjacent lysine residues (K36 and K37) are close to E1286, as also shown by XL-MS data.

Molecular Determinants of Integrin β4 Displacement from the Complex with P1a by CaM

In order to enlighten the regulation mechanism of the integrin β4-P1a complex by Ca^{2+}-CaM at the molecular level, we mimicked binding of Ca^{2+}-CaM to the P1aABD$_{\Delta 22}$/β4Fn12 complex by superimposing the SAXS-derived tentative model of P1aABD/CaM on the crystal structure of the P1aABD$_{\Delta 22}$/β4Fn12 complex (rmsd, 0.77 Å over 206 Cα equivalent atoms). As shown in Figure 7A, binding of Ca^{2+}-CaM to the N-ter extension of P1a results in steric clashes with the second FnIII domain of the integrin β4, implying a disruption of the P1aABD$_{\Delta 22}$/β4Fn12 interaction.

To obtain quantitative understanding of interactions and dissociations of CaM, β4Fn12, and P1aABD, we carried out ITC assays. The binding of β4Fn12 to P1aABD is an entropy-driven reaction with weak affinity (K_d, 41.7 ± 4.2 μM, Figure 7B).

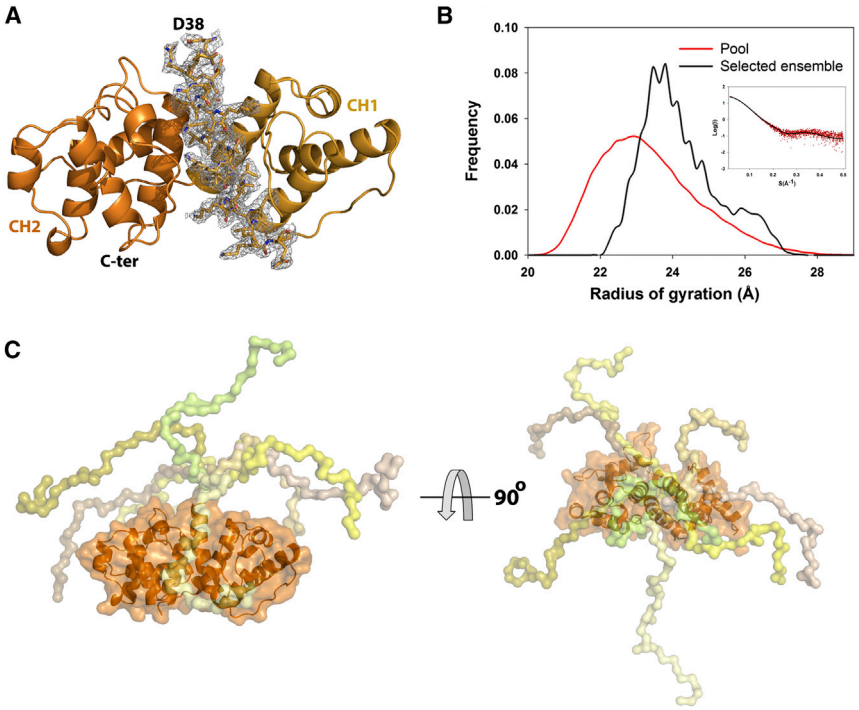

Figure 5. The N-ter Tail of P1a Is Intrinsically Disordered

(A) The crystal structure of P1aABD$_{\Delta 22}$ is displayed in ribbon; CH domains 1 and 2 (CH1 and CH2) are shown in bronze and orange, respectively. The electron density corresponding to 15 residues of N-ter tail (amino acid residues 23–37) is absent in the structure. The electron density map (2Fo-Fc) is contoured at 1.5 σ.

(B) SAXS analysis of the P1aABD. The frequency distributions of R_g generated from EOM compared with the pool (red curve) and the selected ensemble (black curve) are shown. The inset shows the experimental scattering curve (red) and the simulated scattering curve of the selected ensemble by EOM (black).

(C) Eight superimposed models from the selected ensemble, shown in two different orientations (rotated 90° along the *x* axis). The N-ter tail adopts random conformations.

see also Figure S5; Table S2.

Conversely, the binding of Ca^{2+}-CaM to P1aABD is an enthalpy-favored process and more than one order of magnitude stronger (K_d, 4.2 ± 0.4 μM, Figure 7C). No interaction was observed between Ca^{2+}-CaM and β4Fn12 (Figure S6B). In the displacement experiment, in which the P1aABD/β4Fn12 complex was titrated with Ca^{2+}-CaM, the apparent binding affinity of Ca^{2+}-CaM was reduced due to the competitive binding of β4Fn12 to P1aABD (K_d, 7.7 ± 0.7 μM) (Figure 7D), while the enthalpy and entropy changes (ΔH and ΔS) increase as a result of the replacement of an entropic binding with an enthalpic one. The measured binding affinity of Ca^{2+}-CaM P1aABD (K_d, 4.2 ± 0.4 μM) is consistent with the calculated one using the competitive binding model (K_d, 2.3 μM) (Sigurskjold, 2000). Moreover, the binding affinity of Ca^{2+}-CaM to P1aABD$_{\Delta 22}$ (K_d, 2.6 ± 1.0 μM) is comparable with that of P1aABD (Figure S6C). Due to the higher binding affinity of P1aABD to CaM$_{NL}$ (K_d, 10.5 ± 1.1 μM), compared with its affinity to β4Fn12 (K_d, 41.7 μM ± 4.2), CaM$_{NL}$ alone expectedly displaced β4Fn12 from the P1aABD/β4Fn12 complex (Figure S6D).

In addition, we compared the thermodynamics of the β4Fn12 and Ca^{2+}-CaM binding to P1aABD. The formation of the P1aABD/β4Fn12 complex is not enthalpy but entropy driven (Δ*H*, 3.69 kcal/mol, Figure 7B). This indicates that ordered water molecules solvating the binding partners are released upon complex formation (Dunitz, 1994). For the P1aABD/CaM interaction, we showed that the folding of the structurally disordered N-ter tail into an α helix is coupled with binding to Ca^{2+}-CaM. This reaction is entropy unfavorable, as shown by ITC (Figure 7C). However, the enthalpy contribution compensates for the entropy cost to instigate the binding reaction (Figures 7C and 7D) (Dyson and Wright, 2005), which is inferred from the fact that the binding affinity of Ca^{2+}-CaM to P1aABD (K_d, 4.2 μM) is lower than that reported for other binding partners (K_d, 10^{-7}–10^{-11} M) (Crivici and Ikura, 1995).

To explore structural determinants of the preferential affinity of CaM$_{NL}$ for P1a compared with CaM$_{CL}$, we generated a model of the P1aABD$_{\Delta 22}$/CaM$_{CL}$ complex, by superimposing CaM$_{CL}$ (82–146 aa; PDB, 3CLN [Babu et al., 1988]) on the crystal structure of the P1aABD$_{\Delta 22}$/CaM$_{NL}$ complex (rmsd, 0.50 Å over 53 equivalent Cα atoms out of 65). Amino acid residues involved in the interaction interfaces were analyzed by PISA (Krissinel and Henrick, 2007) (Figure S9A). Comparison of the interaction interfaces showed differences in three positions involved in critical stabilizing interactions, which are at the basis of higher affinity of the N-ter lobe: CaM$_{NL}$ Q41/CaM$_{CL}$ E114, CaM$_{NL}$ L18/CaM$_{CL}$ V91, and CaM$_{NL}$ V55/CaM$_{CL}$ A128 (Figure S9B). Although E114 in the C-lobe can potentially form a stronger interaction with the P1aABD R31 residue compared with the corresponding Q41 in the N-lobe, the two bulkier hydrophobic residues in the N-lobe (L18 and V55) contribute to the establishment of a larger hydrophobic interface with plectin than the equivalent C-lobe residues (V91 and A128) (Figure S9B). The total interface area of CaM$_{NL}$ (635 Å^2, 14.9% of the solvent accessible surface area) is larger than that of CaM$_{CL}$ (618 Å^2, 13.4% of the solvent accessible surface area) (Table S4).

We further compared the intermolecular interfaces of the P1aABD$_{\Delta 22}$/CaM$_{NL}$ and P1aABD/β4Fn12 complexes. Probability measures $P_{\Delta G,IF}$ of specific interfaces were derived from the gain in solvation energy upon complex formation, with $P_{\Delta G,IF} > 0.5$ pointing to hydrophilic/unspecific and $P_{\Delta G,IF} < 0.5$ to hydrophobic/specific interfaces using PISA. In the case of P1aABD$_{\Delta 22}$/CaM$_{NL}$, the $P_{\Delta G,IF}$ values (<0.15) are in the range of probabilities derived from typical protein interfaces (0.1–0.4). In the case of P1aABD/β4Fn12, however, the $P_{\Delta G,IF}$ value close to 0.6 suggests a less specific interaction, with concomitantly smaller solvation energy gain (Table S4). These data collectively show that CaM$_{NL}$ is the high-affinity ligand of P1aABD. The finely tuned hydrophobic interactions of CaM$_{NL}$ with the N-ter tail of P1a lead to its capacity to disrupt the weaker and less specific interaction between P1a and integrin β4.

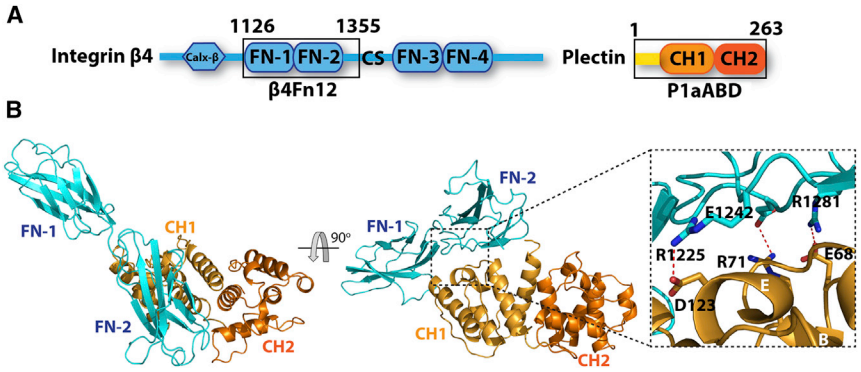

Figure 6. Structure of P1aABD/β4Fn12 Complex

(A) Schematic illustrations of integrin β4 and P1a fragments used in the experiments (boxed areas).
(B) The crystal structure of the $P1aABD_{\Delta 22}$/β4Fn12 complex is shown in two orientations. β4Fn12 is displayed in cyan, and the CH1 and CH2 of the $P1aABD_{\Delta 22}$ are displayed in bronze and orange, respectively. The binding interface comprises three salt bridges between P1a and integrin β4; D123/R1225 (2.60 Å), R71/E1242 (3.04 Å), and E68/R1281 (2.57 Å).
see also Figures S7 and S8; Table S2.

DISCUSSION

Specific subcellular localizations have been identified for several plectin isoforms (Castanon et al., 2013). Nevertheless, few isoform-specific binding partners of these variants have been reported. Our results showed that Ca^{2+}-CaM binds specifically to the P1a isoform, in particular to the ten residues of the isoform-specific N-ter tail, directly preceding the isoform-conserved ABD. The role of the 22 isoform-specific amino acid residues preceding the CaM binding site is still unknown. However, the specific localization of P1a to HDs suggests that this part of the isoform-specific sequence most likely harbors a signal for targeting of P1a into HDs. Plectin isoform diversity suggests that the function and nature of the plectin interactions with binding partners will vary, depending on both interaction partners and specific N-ter extensions.

Obviously, the strength of the interactions as measured in vitro may well vary from those in vivo, in which the interaction of P1a with integrin β4 is further stabilized by other interaction sites (Walko et al., 2014), contributing to localization of P1aABD in the vicinity of β4Fn2, thus increasing the probability of these domains to interact. In any case, the interaction of P1aABD with Ca^{2+}-CaM displays affinity that is an order of magnitude higher than that with β4Fn12, and these differential affinities are crucial for the regulation of HD disassembly. Moreover, dimer and higher oligomeric forms of P1a contribute to the stability of HDs (Walko et al., 2011) and might have additional impact on HD disassembly regulated by Ca^{2+}-CaM.

In addition to its role in regulating the interaction of P1a and integrin β4, Kostan et al showed that Ca^{2+}-CaM also prevents plectin ABD from binding to F-actin (Kostan et al., 2009). To understand the molecular mechanism of this process, we superimposed the SAXS structure of the P1aABD/CaM complex on the homologous CH1 domain of α-actinin bound to F-actin (PDB, 3LUE) (Galkin et al., 2010) (rmsd, 0.54 Å over 98 equivalent Cα atoms). Superimposition of the P1aABD/CaM model onto the ABD of α-actinin bound to F-actin (Galkin et al., 2010) showed that CaM does not directly affect the actin binding sites of CH1 (Bresnick et al., 1990; Levine et al., 1990) but rather produces steric clashes between Ca^{2+}-CaM and F-actin (Figure 8), which likely explains the inability of this complex to bind F-actin.

The results presented here support and extend the previously proposed model of HD disassembly (Kostan et al., 2009) and explain isoform specificity of P1a binding to Ca^{2+}-CaM. In our extended model (Figure 9), the P1a/integrin β4 complex is maintained at low cytosolic calcium concentrations in HDs. In this complex, P1a and integrin β4 interact via the isoform-independent interface. The N-ter isoform-specific tail of P1a is disordered in this complex and is not involved in the interaction. Upon increased cytosolic Ca^{2+} concentrations during keratinocyte differentiation or wound healing, activated CaM binds to the N-ter tail of P1a via its N-lobe, while the C-lobe plays an auxiliary role in this interaction. The N-ter tail folds into an α helix upon CaM binding to P1a, leading to a steric clash between both the N- and C-terminal lobes of CaM and β4Fn12, which in turn instigates the displacement of integrin β4 from P1a.

For HD dynamics, being structurally disordered is an essential property of the P1a N-ter tail for three main reasons. First, although the N-ter extension does not contribute to the complex formation with integrin β4, an α helix in place of a structurally disordered peptide would generate a steric clash with integrin β4. Second, being structurally disordered in complex with integrin β4 enables exploration of a large conformational space, facilitating the recruitment of Ca^{2+}-CaM upon increased cytosolic calcium levels. Intrinsically disordered regions provide conformational fluctuations, which can facilitate intermolecular interactions, forming complexes with high specificity and relatively low affinity. This is critical for processes in which not only specific association but also subsequent dissociation of binding partners is required (Tompa and Csermely, 2004). Third, binding to Ca^{2+}-CaM leads to the formation of an α helix, which suitably positions Ca^{2+}-CaM to displace integrin β4 and F-actin from the complex with plectin.

This study contributes to the understanding of molecular mechanisms regulating the functional states of HDs. Using a combination of structural, mutational, biophysical and in vivo studies, we show that the binding of Ca^{2+}-CaM to the N-ter extension of P1a is involved in disruption of the plectin/integrin β4 and plectin/F-actin complexes by shunting integrin β4 and F-actin, without directly competing for the binding site. We further showed that the interaction of plectin with Ca^{2+}-CaM is isoform specific, while the interaction with integrin β4 is not, implying that the main function of the N-ter tail is regulation of P1a interaction with integrin β4 and F-actin, and not direct binding to these partners.

Finally, several cytoskeletal proteins of the spectrin superfamily (spectrin, utrophin, dystrophin, β-actinin) harbor EF-hand motifs, which may play important roles in regulating cytoskeletal

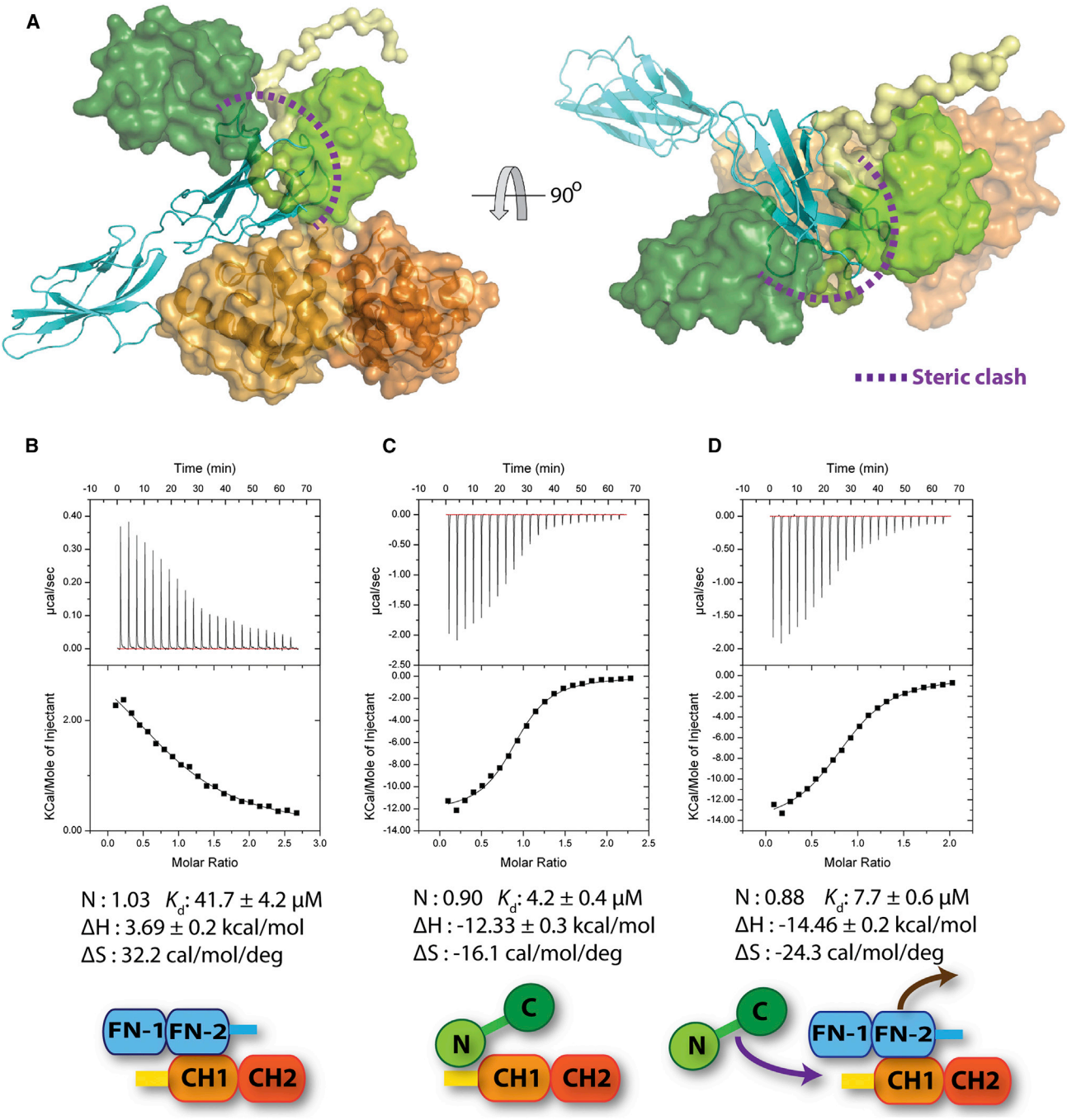

Figure 7. Displacement of β4Fn12 from the β4Fn12/P1aABD Complex by Ca^{2+}-CaM

(A) The SAXS-derived tentative model of the CaM/P1aABD complex (for detail see Figure 4E), shown as surface, was superimposed on the ABD of the plectin of the $P1aABD_{\Delta 22}$/β4Fn12 complex, shown as ribbon. Steric clashes of Fn2 domain with CaM/P1aABD are indicated with a purple dashed line.

(B–D) Displacement of β4Fn12 by Ca^{2+}-CaM as analyzed by ITC. (B) P1aABD (0.08 mM) was titrated with β4Fn12 (0.8 mM) and exhibited entropy-driven binding. (C) P1aABD (0.1 mM) was titrated with CaM (1 mM). CaM bound to P1aABD with a higher affinity than β4Fn12. (D) For the displacement assay, 1 mM CaM was injected into the sample cell containing 0.1 mM P1aABD and 0.1 mM β4Fn12. Data are expressed as mean values ± SD.

see also Figure S6.

interactions near the plasma membranes (Bennett and Healy, 2008). The studies on titin-α-actinin (Young and Gautel, 2000) and recent studies on spectrin-ankyrin, actin, and protein 4.2 (Korsgren and Lux, 2010; Korsgren et al., 2010) suggest that these interactions are governed by a pseudoligand mechanism. Furthermore, Ca^{2+}-CaM was reported to regulate filamin A and utrophin interactions with F-actin (Nakamura et al., 2005; Winder and Kendrick-Jones, 1995). Our study provides the first

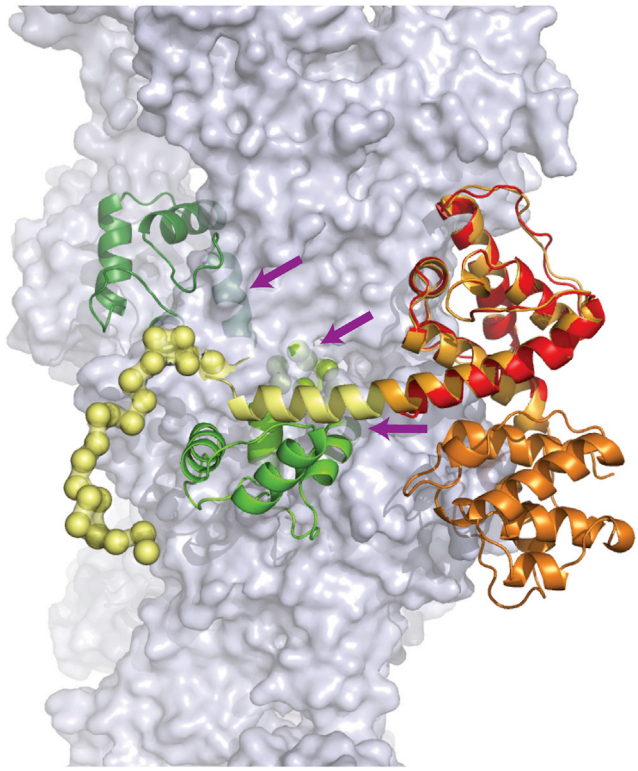

Figure 8. Ca^{2+}-CaM Regulates Binding of P1a to F-actin
The SAXS-derived tentative model of the P1aABD/CaM complex was superimposed to the CH1 domain of α-actinin (red), which is bound to F-actin (light gray, PDB: 3LUE). The steric clash between the P1aABD/CaM complex and F-actin is shown by purple arrows.

structural insight into a mechanism of Ca^{2+}-CaM-regulated interactions of an actin binding protein. Although the regulatory mechanics depicted above might differ, this analysis could serve as a blueprint for future studies aiming at understanding how Ca^{2+}/CaM or EF-hand motifs regulate interactions in actin-associated proteins.

EXPERIMENTAL PROCEDURES

Protein Cloning, Expression, Purification, and Crystallization

Proteins were expressed as His_6-fusions in *Escherichia coli* and purified via Ni-NTA agarose and SEC as described in the Supplemental Materials and Methods.

Structure Determination of the P1aABD$_{\Delta22}$/CaM$_{NL}$ and P1aABD$_{\Delta22}$/β4Fn12 Complex

Equimolar mixture of P1aABD$_{\Delta22}$ and CaM$_{NL}$ was applied to an SEC column and elution peak containing the complex concentrated to 11 mg/ml. Crystals were grown by the hanging-drop vapor diffusion method at 4°C from a solution containing 0.1 M Bis-Tris (pH 6.5), 0.2 M $MgCl_2$, and 13% PEG 8000. The structure was solved by molecular replacement using human plectin ABD (PDB, 1MB8) (Garcia-Alvarez et al., 2003) and the N-ter lobe of Ca^{2+}-CaM (PDB, 3CLN) (Babu et al., 1988) as search models.

Crystals of P1aABD$_{\Delta22}$ were grown by the sitting-drop vapor diffusion method at 22°C from a solution containing 50 mM monobasic potassium phosphate and 20% PEG 8000. The structure was solved by molecular replacement using human plectin ABD (PDB, 1MB8) (Garcia-Alvarez et al., 2003).

An equimolar mixture of P1aABD$_{\Delta22}$ and β4Fn12 was concentrated to 12 mg/ml. Crystals of the protein complex were grown at 22°C using hanging-drop vapor diffusion, from a solution containing 20 mM HEPES-NaOH (pH 6.5), 150 mM sodium formate, 7.5% PEG 550 MME, and 3% sucrose. Crystals were dehydrated by transferring coverslips to reservoirs containing the crystallization solution with increasing concentrations of PEG 550 MME. The structure was solved by molecular replacement using plectin ABD (PDB, 1MB8) and integrin β4 fragment (PDB, 3F7Q) as search models (de Pereda et al., 2009).

Diffraction data were collected at the beamlines ID14-1, ID14-4, and ID23-2 at ESRF (European Synchrotron Radiation Facility, Grenoble, France). Details on data collection, processing, structure determination, and refinement are described in the Supplemental Materials and Methods and in Table 1.

ITC

All protein samples were dialyzed against the ITC buffer (20 mM HEPES-NaOH [pH 7.5], 150 mM NaCl, and 5 mM $CaCl_2$) overnight at 4°C. ITC was performed at 25°C or 30°C using an iTC_{200} Microcalorimeter (MicroCal, GE Healthcare). Thermodynamic parameters were obtained by fitting the one-site binding model or competitive binding model using the program Origin 7. The heat of dilution into buffer was subtracted from each reaction or the final titration point was used to estimate the reference baseline.

SAXS, Crosslinking, and Mass Spectrometry Analyses

SAXS data were collected on beamline X3 at EMBL (European Molecular Biology Laboratory) c/o DESY (Deutsches Elektronen-Synchrotron) (Hamburg, Germany) for WT, NEECK, and PIP2 mutants at three different concentrations and analyzed using the ATSAS package program (Petoukhov et al., 2012) following standard procedures.

Crosslinking experiments were performed using both a one-step and a two-step protocol. For the one-step method, with EDC and sulfo-NHS, bands from SDS-PAGE were excised, trypsinized, and analyzed by high-resolution LC-MS/MS. Details are described in the Supplemental Materials and Methods.

Pull-Down Assay

All plectin constructs were prepared at a concentration of 5 μM in buffer P (20 mM Tris-HCl [pH 7.5], 150 mM NaCl, 0.05% Tween 20). Plectin samples (1 ml) were mixed with 50 μl of CaM-Sepharose 4B beads (GE Healthcare) supplemented with either 5 mM $CaCl_2$ or 1 mM EDTA. The samples were incubated for 2 hr at room temperature, followed by centrifugation at 3,000 x *g* for 2 min. Beads were washed with 1.5 ml of buffer P three times and incubated with an SDS-PAGE sample buffer at 95°C for 10 min to elute bound samples.

FRET Experiments

Rat bladder carcinoma 804G cells were grown in DMEM (Sigma Aldrich). FRET was measured by the acceptor photobleaching method as previously described (Stanek and Neugebauer, 2004) using the Leica SP5 confocal microscope. Details of the procedures are described in the Supplemental Materials and Methods.

ACCESSION NUMBERS

The atomic coordinates of the P1aABD$_{\Delta22}$, P1aABD$_{\Delta22}$/CaM$_{NL}$, and P1aABD$_{\Delta22}$/β4Fn12 complexes are deposited in the PDB under codes: 4Q59, 4Q57, and 4Q58, respectively.

SUPPLEMENTAL INFORMATION

Supplemental Information includes Supplemental Materials and Methods, four tables, and nine figures and can be found with this article online at http://dx.doi.org/10.1016/j.str.2015.01.011.

AUTHOR CONTRIBUTIONS

K.D.C. and G.W. conceived the project. J.-G.S. performed all structural and biochemical experiments and analyzed the data. F.D. and B.K. performed the XL-MS experiments and analyzed the data. E.d.A.R., P.K., and D.S. helped with analysis of SAXS data. M.G. performed FRET experiments and analyzed the data. I.G. helped with X-ray diffraction data collection and structure

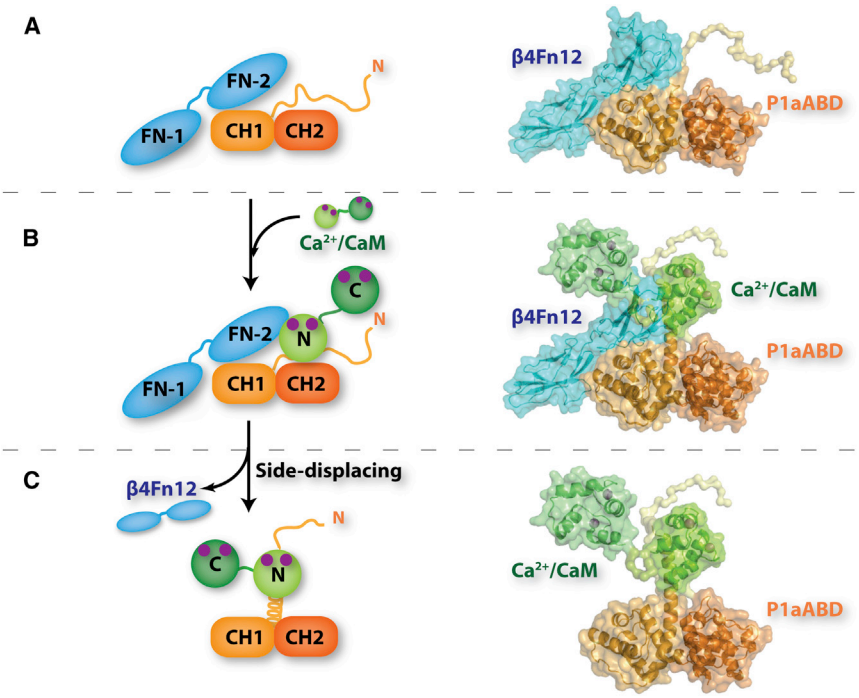

Figure 9. Model for the CaM-Driven Disruption of the P1aABD/β4Fn12 Complex

(A) At low cytosolic calcium concentrations, the P1a/integrin α6β4 complex is maintained in HDs.

(B) Increased cytosolic calcium concentration, during differentiation or wound healing, leads to activation of CaM (Ca^{2+}-CaM). CaM in its active form binds to the structurally disordered N-ter tail of P1a via its N-ter lobe.

(C) CaM binding leads to the folding of the N-ter tail of P1a into an α helix. The steric clash caused by CaM bound to the α helix results in shunting of integrin β4 from the complex, contributing to HD disassembly.

refinement. J.-G.S., J.K., and K.D.C. prepared the figures and wrote the manuscript. All authors commented on the manuscript.

ACKNOWLEDGMENTS

K.D.C.'s research was supported by the Austrian Science Fund (FWF) through Grant Number W1221 DK, by the Federal Ministry of Economy, Family and Youth through the initiative "Laura Bassi Centres of Expertise" Funding Center of Optimized Structural Studies, Grant Number 253275, and by the Austrian Science Fund Grant (FWF) Number P22276. M.G. received support from Ministry of Education, Youth and Sports Grant Number 7AMB13AT012 and Operational Programme Research and Development for Innovation Grant Number CZ.1.05/1.1.00/02.0109 BIOCEV. The work of B.W. was supported by the Deutsche Forschungsgemeinschaft, Grant Number FOR1352 and by the Excellence Initiative of the German Federal & State Governments, Grant Number EXC 294 BIOSS Centre for Biological Signaling Studies). The research leading to these results has received funding from the European Community's Seventh Framework Programme (FP7/2007-2013) under BioStruct-X (Grant Agreement N°283570). We thank staff of X-ray beamlines at ESRF in Grenoble, SAXS beamline X33 (DESY, Hamburg), and SWING (Soleil, Saint-Aubin) for their excellent support. We are grateful to Oliviero Carugo (University of Vienna and University of Pavia) and Brooke Morriswood (University of Vienna, Max F. Perutz Laboratories) for critical reading of the manuscript.

Received: October 18, 2014
Revised: December 24, 2014
Accepted: January 6, 2015
Published: February 19, 2015

REFERENCES

Andra, K., Lassmann, H., Bittner, R., Shorny, S., Fassler, R., Propst, F., and Wiche, G. (1997). Targeted inactivation of plectin reveals essential function in maintaining the integrity of skin, muscle, and heart cytoarchitecture. Genes Dev. *11*, 3143–3156.

Andra, K., Kornacker, I., Jorgl, A., Zorer, M., Spazierer, D., Fuchs, P., Fischer, I., and Wiche, G. (2003). Plectin-isoform-specific rescue of hemidesmosomal defects in plectin (-/-) keratinocytes. J. Invest. Dermatol. *120*, 189–197.

Babu, Y.S., Bugg, C.E., and Cook, W.J. (1988). Structure of calmodulin refined at 2.2 A resolution. J. Mol. Biol. *204*, 191–204.

Bennett, V., and Healy, J. (2008). Organizing the fluid membrane bilayer: diseases linked to spectrin and ankyrin. Trends Mol. Med. *14*, 28–36.

Bernado, P., Mylonas, E., Petoukhov, M.V., Blackledge, M., and Svergun, D.I. (2007). Structural characterization of flexible proteins using small-angle X-ray scattering. J. Am. Chem. Soc. *129*, 5656–5664.

Borradori, L., and Sonnenberg, A. (1999). Structure and function of hemidesmosomes: more than simple adhesion complexes. J. Invest. Dermatol. *112*, 411–418.

Bresnick, A.R., Warren, V., and Condeelis, J. (1990). Identification of a short sequence essential for actin binding by *Dictyostelium* ABP-120. J. Biol. Chem. *265*, 9236–9240.

Castanon, M.J., Walko, G., Winter, L., and Wiche, G. (2013). Plectin-intermediate filament partnership in skin, skeletal muscle, and peripheral nerve. Histochem. Cell Biol. *140*, 33–53.

Chattopadhyaya, R., Meador, W.E., Means, A.R., and Quiocho, F.A. (1992). Calmodulin structure refined at 1.7 A resolution. J. Mol. Biol. *228*, 1177–1192.

Crivici, A., and Ikura, M. (1995). Molecular and structural basis of target recognition by calmodulin. Annu. Rev. Biophys. Biomol. Struct. *24*, 85–116.

de Pereda, J.M., Lillo, M.P., and Sonnenberg, A. (2009). Structural basis of the interaction between integrin alpha6beta4 and plectin at the hemidesmosomes. EMBO J. *28*, 1180–1190.

Dunitz, J.D. (1994). The entropic cost of bound water in crystals and biomolecules. Science *264*, 670.

Dyson, H.J., and Wright, P.E. (2005). Intrinsically unstructured proteins and their functions. Nat. Rev. Mol. Cell Biol. *6*, 197–208.

Frijns, E., Sachs, N., Kreft, M., Wilhelmsen, K., and Sonnenberg, A. (2010). EGF-induced MAPK signaling inhibits hemidesmosome formation through phosphorylation of the integrin {beta}4. J. Biol. Chem. *285*, 37650–37662.

Frijns, E., Kuikman, I., Litjens, S., Raspe, M., Jalink, K., Ports, M., Wilhelmsen, K., and Sonnenberg, A. (2012). Phosphorylation of threonine 1736 in the C-terminal tail of integrin beta4 contributes to hemidesmosome disassembly. Mol. Biol. Cell *23*, 1475–1485.

Fuchs, P., Zorer, M., Rezniczek, G.A., Spazierer, D., Oehler, S., Castanon, M.J., Hauptmann, R., and Wiche, G. (1999). Unusual 5′ transcript complexity of plectin isoforms: novel tissue-specific exons modulate actin binding activity. Hum. Mol. Genet. *8*, 2461–2472.

Galkin, V.E., Orlova, A., Salmazo, A., Djinovic-Carugo, K., and Egelman, E.H. (2010). Opening of tandem calponin homology domains regulates their affinity for F-actin. Nat. Struct. Mol. Biol. *17*, 614–616.

Garcia-Alvarez, B., Bobkov, A., Sonnenberg, A., and de Pereda, J.M. (2003). Structural and functional analysis of the actin binding domain of plectin suggests alternative mechanisms for binding to F-actin and integrin beta4. Structure *11*, 615–625.

Geerts, D., Fontao, L., Nievers, M.G., Schaapveld, R.Q., Purkis, P.E., Wheeler, G.N., Lane, E.B., Leigh, I.M., and Sonnenberg, A. (1999). Binding of integrin alpha6beta4 to plectin prevents plectin association with F-actin but does not interfere with intermediate filament binding. J. Cell Biol. *147*, 417–434.

Georges-Labouesse, E., Messaddeq, N., Yehia, G., Cadalbert, L., Dierich, A., and Le Meur, M. (1996). Absence of integrin alpha 6 leads to epidermolysis bullosa and neonatal death in mice. Nat. Genet. *13*, 370–373.

Green, K.J., and Jones, J.C. (1996). Desmosomes and hemidesmosomes: structure and function of molecular components. FASEB J. *10*, 871–881.

Heidorn, D.B., and Trewhella, J. (1988). Comparison of the crystal and solution structures of calmodulin and troponin C. Biochemistry *27*, 909–915.

Ishida, T., and Kinoshita, K. (2007). PrDOS: prediction of disordered protein regions from amino acid sequence. Nucleic Acids Res. *35*, W460–W464.

Konarev, P.V., Volkov, V.V., Sokolova, A.V., Koch, M.H.J., and Svergun, D.I. (2003). PRIMUS: a Windows PC-based system for small-angle scattering data analysis. J. Appl. Crystallogr. *36*, 1277–1282.

Korsgren, C., and Lux, S.E. (2010). The carboxyterminal EF domain of erythroid alpha-spectrin is necessary for optimal spectrin-actin binding. Blood *116*, 2600–2607.

Korsgren, C., Peters, L.L., and Lux, S.E. (2010). Protein 4.2 binds to the carboxyl-terminal EF-hands of erythroid alpha-spectrin in a calcium- and calmodulin-dependent manner. J. Biol. Chem. *285*, 4757–4770.

Kostan, J., Gregor, M., Walko, G., and Wiche, G. (2009). Plectin isoform-dependent regulation of keratin-integrin alpha6beta4 anchorage via Ca^{2+}/calmodulin. J. Biol. Chem. *284*, 18525–18536.

Krissinel, E., and Henrick, K. (2007). Inference of macromolecular assemblies from crystalline state. J. Mol. Biol. *372*, 774–797.

Levine, B.A., Moir, A.J., Patchell, V.B., and Perry, S.V. (1990). The interaction of actin with dystrophin. FEBS Lett. *263*, 159–162.

Litjens, S.H., de Pereda, J.M., and Sonnenberg, A. (2006). Current insights into the formation and breakdown of hemidesmosomes. Trends Cell Biol. *16*, 376–383.

Nakamura, F., Hartwig, J.H., Stossel, T.P., and Szymanski, P.T. (2005). Ca^{2+} and calmodulin regulate the binding of filamin A to actin filaments. J. Biol. Chem. *280*, 32426–32433.

Niessen, C.M., Hulsman, E.H., Oomen, L.C., Kuikman, I., and Sonnenberg, A. (1997). A minimal region on the integrin beta4 subunit that is critical to its localization in hemidesmosomes regulates the distribution of HD1/plectin in COS-7 cells. J. Cell Sci. *110*, 1705–1716.

Novotny, I., Blazikova, M., Stanek, D., Herman, P., and Malinsky, J. (2011). In vivo kinetics of U4/U6.U5 tri-snRNP formation in Cajal bodies. Mol. Biol. Cell *22*, 513–523.

Petoukhov, M.V., Franke, D., Shkumatov, A.V., Tria, G., Kikhney, A.G., Gajda, M., Gorba, C., Mertens, H.D.T., Konarev, P.V., and Svergun, D.I. (2012). New developments in the ATSAS program package for small-angle scattering data analysis. J. Appl. Crystallogr. *45*, 342–350.

Rabinovitz, I., Tsomo, L., and Mercurio, A.M. (2004). Protein kinase C-alpha phosphorylation of specific serines in the connecting segment of the beta 4 integrin regulates the dynamics of type II hemidesmosomes. Mol. Cell. Biol. *24*, 4351–4360.

Rhoads, A.R., and Friedberg, F. (1997). Sequence motifs for calmodulin recognition. FASEB J. *11*, 331–340.

Sigurskjold, B.W. (2000). Exact analysis of competition ligand binding by displacement isothermal titration calorimetry. Anal. Biochem. *277*, 260–266.

Stanek, D., and Neugebauer, K.M. (2004). Detection of snRNP assembly intermediates in Cajal bodies by fluorescence resonance energy transfer. J. Cell Biol. *166*, 1015–1025.

Svergun, D., Barberato, C., and Koch, M.H.J. (1995). CRYSOL–a program to evaluate x-ray solution scattering of biological macromolecules from atomic coordinates. J. Appl. Crystallogr. *28*, 768–773.

Tamura, R.N., Rozzo, C., Starr, L., Chambers, J., Reichardt, L.F., Cooper, H.M., and Quaranta, V. (1990). Epithelial integrin alpha 6 beta 4: complete primary structure of alpha 6 and variant forms of beta 4. J. Cell Biol. *111*, 1593–1604.

Tennenbaum, T., Li, L., Belanger, A.J., De Luca, L.M., and Yuspa, S.H. (1996). Selective changes in laminin adhesion and alpha 6 beta 4 integrin regulation are associated with the initial steps in keratinocyte maturation. Cell Growth Differ. *7*, 615–628.

Tompa, P., and Csermely, P. (2004). The role of structural disorder in the function of RNA and protein chaperones. FASEB J. *18*, 1169–1175.

van der Neut, R., Krimpenfort, P., Calafat, J., Niessen, C.M., and Sonnenberg, A. (1996). Epithelial detachment due to absence of hemidesmosomes in integrin beta 4 null mice. Nat. Genet. *13*, 366–369.

Walko, G., Vukasinovic, N., Gross, K., Fischer, I., Sibitz, S., Fuchs, P., Reipert, S., Jungwirth, U., Berger, W., Salzer, U., et al. (2011). Targeted proteolysis of plectin isoform 1a accounts for hemidesmosome dysfunction in mice mimicking the dominant skin blistering disease EBS-Ogna. PLoS Genet. *7*, e1002396.

Walko, G., Castanon, M.J., and Wiche, G. (2014). Molecular architecture and function of the hemidesmosome. Cell Tissue Res. Published online December 9, 2014. http://dx.doi.org/10.1007/s00441-014-2061-z.

Wilhelmsen, K., Litjens, S.H., Kuikman, I., Margadant, C., van Rheenen, J., and Sonnenberg, A. (2007). Serine phosphorylation of the integrin beta4 subunit is necessary for epidermal growth factor receptor induced hemidesmosome disruption. Mol. Biol. Cell *18*, 3512–3522.

Winder, S.J., and Kendrick-Jones, J. (1995). Calcium/calmodulin-dependent regulation of the NH2-terminal F-actin binding domain of utrophin. FEBS Lett. *357*, 125–128.

Young, P., and Gautel, M. (2000). The interaction of titin and alpha-actinin is controlled by a phospholipid-regulated intramolecular pseudoligand mechanism. EMBO J. *19*, 6331–6340.

Structure, Volume *23*

Supplemental Information

Structural Insights into Ca^{2+}-Calmodulin Regulation of Plectin 1a-Integrin β4 Interaction in Hemidesmosomes

Jae-Geun Song, Julius Kostan, Friedel Drepper, Bettina Knapp, Euripedes de Almeida Ribeiro, Jr., Petr V. Konarev, Irina Grishkovskaya, Gerhard Wiche, Martin Gregor, Dmitri I. Svergun, Bettina Warscheid, and Kristina Djinović-Carugo

Supplementary information

Structural insights into Ca^{2+}/calmodulin regulation of plectin 1a - integrin β4 interaction in hemidesmosomes

Jae-Geun Song[1], Julius Kostan[1], Friedel Drepper[2], Bettina Knapp[2], Euripedes de Almeida Ribeiro Jr[1], Petr V. Konarev[3], Irina Grishkovskaya[1], Gerhard Wiche[4], Martin Gregor[5], Dmitri I. Svergun[3], Bettina Warscheid[2] and Kristina Djinović-Carugo[1,6]

[1]Department of Structural and Computational Biology, Max F. Perutz Laboratories, University of Vienna, Campus Vienna Biocenter 5, A-1030 Vienna, Austria

[2]Department of Functional Proteomics and Biochemistry, Institute of Biology II and BIOSS Centre for Biological Signaling Studies, University of Freiburg, Schaenzlestrasse 1, D-79104 Freiburg, Germany

[3]EMBL-Hamburg c/o DESY, Notkestrasse 85, D-22603, Hamburg, Germany

[4]Department of Biochemistry and Cell Biology, Max F. Perutz Laboratories, University of Vienna, A-1030 Vienna, Dr. Bohrgasse 9, Austria

[5]Department of Integrative Biology, Institute of Molecular Genetics of the ASCR, Vídeňská 1083, Prague 4, CZ-14220, Czech Republic

[6]Department of Biochemistry, Faculty of Chemistry and Chemical Technology, University of Ljubljana, Aškerčeva 5, SI-1000 Ljubljana, Slovenia

*Corresponding author: Kristina Djinović-Carugo (e-mail: kristina.djinovic@univie.ac.at)

Supplementary Information

Materials and Methods

Protein Cloning, Expression and Purification

The murine plectin construct (P1aABD, 1-263) contains the N-ter tail and the actin-binding domain (ABD) of plectin isoform 1a (Uniprot accession number: **Q9QXS1-3**). The truncation mutants of P1aABD were generated to express various lengths of the N-ter segment, and were named P1aABD$_{\Delta 11}$ (12-263), P1aABD$_{\Delta 22}$ (23-263), P1aABD$_{\Delta 32}$ (33-263), and P1aABD$_{\Delta 37}$ (38-263). The integrin β4 construct termed β4Fn12 (1126-1355) comprises the first pair of fibronectin type III domains including a part of the connecting segment (CS) of integrin β4 (Niessen et al., 1997) and was cloned using the cDNA of human integrin β4 (Rezniczek et al., 1998). The full-length calmodulin construct (CaM, 1-148) and its truncated versions encoding the N-ter and C-terminal lobes (CaM$_{NL}$ (6-73) and CaM$_{CL}$ (83-148), respectively) were prepared by cloning the entire human CaM gene III (Uniprot accession number: **P62158**). To generate constructs for heterologous expression in *E. coli*, plectin, calmodulin, and integrin β4 cDNAs were cloned into the pETM-14 vector, which encodes an N-ter His$_6$-tag and the 3C protease cleavage site.

An expression plasmid CaM-YFP (pMG13) encoding C-terminally EYFP-tagged calmodulin was generated by subcloning cDNA for human CaM gene III (a gift from D.C. Chang, Hong Kong University, China) into pEGFP-N2 -based plasmid (Clontech Laboratories, Inc.), where enhanced GFP had been replaced by EYFP (pEYFP). For cloning P1aABD-CFP (pMG39) encoding C-terminally ECFP-tagged plectin 1aABD, cDNA encoding a plectin fragment corresponding to exons 1a-8 (1aABD) (Kostan et al., 2009) was subcloned into pECFP-N2 plasmid which was generated using the same cloning strategy as pEYFP (see above). The YFP- and CFP-encoding plasmids were kindly provided by R. Tsien (University of California, San Diego, USA). The expression plasmid encoding CFP-YFP fusion was gift from D. Stanek (Institute of Molecular Genetics, Academy of Sciences of the Czech Republic, Czech Republic).

Oligonucleotide primers were designed to mutate two hydrophobic residues (Leu25Asp and Val29Asp) in the N-ter tail of plectin 1a. The PCR was carried out using the pMG39 vector mentioned above and the mutagenesis oligonucleotide primers (LVDD-F: 5‘ AGCTCAGAGGACAACGACTACCTGGCTGACCTCAGA GCCTCCGAG and LVDD-R: 5’ CTCGGAGGCTCTGAGGTCAGCCAGGTAGTCGTTGTCCTCTGAGCT). The amplified vector was incubated with *Dpn*I at 37 °C for 1 h to digest the template plasmid, followed by the transformation of competent *E.coli* DH5α cells.

The proteins were overexpressed in *E. coli* Rosetta2 (DE3) pLysS cells at 18 °C for 16 h after IPTG induction once the population reached an OD 600 of 0.6. Cells were lysed by sonication and protein purification was carried out using a 5 ml HisTrap HP column (GE Healthcare). To remove the His_6-tag, proteins were dialyzed against buffer containing 20 mM Tris-HCl pH 7.5, 500 mM NaCl, 0.1 mM EDTA, and 2 mM β-mercaptoethanol, and incubated with GST-3C protease. After a second nickel-affinity chromatography step, used to remove uncleaved protein, cleaved protein was further purified by gel filtration using a Superdex 75 16/600 column (GE Healthcare) equilibrated with 20 mM Tris-HCl pH 7.5, 150 mM NaCl, and 0.1 mM EDTA. To remove GST-3C protease from the sample, 5ml GSTrap HP column (GE Healthcare) was connected in series with the gel filtration column.

Small Angle X-ray Scattering (SAXS)

SAXS experiments on the P1aABD/CaM complex were performed using the SAXS beamline X33 at DESY (Hamburg, Germany) (Blanchet et al., 2012). The protein complex was purified by size-exclusion chromatography using a Superdex 75 16/60 column (GE Healthcare) after mixing P1aABD and CaM in an equal molar ratio. Protein samples were prepared in three different concentrations (3.5, 6.0, and 8.4 mg/ml) in the SAXS buffer (20 mM Tris-HCl pH 7.5, 150 mM NaCl, 5 mM $CaCl_2$, and 1 mM DTT). Structural parameters, zero-angle intensity (I(0)) and radius of gyration (Rg), from the Guinier plot were calculated using PRIMUS (Konarev et al., 2003). The program GNOM was employed to generate the pair distribution curve for determining the maximum dimension (D_{max}) and to obtain Rg and I(0) values (Svergun, 1992). *Ab initio* shape determination was computed by the program DAMMIF (Franke and Svergun, 2009) and generated dummy models were averaged using the program DAMAVER (Volkov and Svergun, 2003). Rigid-body modeling of the complex was performed by the program CORAL (Petoukhov et al., 2012) employing two subunits - one is the crystal structure of the $P1aABD_{\Delta 22}/CaM_{NL}$ complex and the other is the crystal structure of CaM_{CL} (83-148, PDB: 3CLN) (Babu et al., 1988), which was combined with an *ab initio* approach to model missing residues (1-21 residues of P1aABD and 74-82 residues of CaM).

SAXS data of the P1aABD/β4Fn12 complex were collected at SWING beamline in the synchrotron SOLEIL (Saint-Aubin, France) (David and Perez, 2009) and processed using the program Foxtrot. The protein complex was prepared by mixing P1aABD and β4Fn12 in an equal molar ratio with three concentration

series (2.4, 4.5, and 6.9 mg/ml) containing the SAXS buffer lacking $CaCl_2$. *Ab initio* structure determination of the P1aABD/β4Fn12 complex was performed in the same way as for the P1aABD/CaM complex. The program OLIGOMER (Konarev et al., 2003) was employed to calculate the volume fraction of the P1aABD/β4Fn12 complex in solution to account for its partial dissociation for the concentrations used. The residues missing in the crystal structure of the $P1aABD_{\Delta 22}$/β4Fn12 complex (1-37 residues of P1aABD and 1321-1355 residues of β4Fn12) were modeled by the program BUNCH (Petoukhov et al., 2012) before generating form factors for OLIGOMER analyses.

EOM (Ensemble optimization method) was employed to assess the flexibility of the N-ter tail of P1a (Bernado et al., 2007). Three concentrations of P1aABD samples (3.0, 4.5, and 6.0 mg/ml) were measured at the SAXS beamline X33 at the DORIS III storage ring, DESY (Hamburg, Germany) (Blanchet et al., 2012). The random pool of 10,000 conformers was generated to model the N-ter tail using the crystal structure of plectin ABD as a constraint. 50 models in the pool were selected to calculate the averaged scattering intensity (termed as selected ensemble), which was fitted to experimental data. Rg distributions against the frequency of occurrence were analyzed and compared between the pool and the selected ensemble.

Cross-Linking and Mass Spectrometry Analyses

Cross-linking experiments were performed using both a one-step and a two-step protocol. For the one-step method, 2 mM 1-ethyl-3-(3-dimethylaminopropyl)carbodiimide (EDC) and 5 mM N-hydroxysulfo-succinimide (sulfo-NHS) were added to the mixture of P1aABD and CaM (5 µM each prepared in the reaction buffer I consisting of 0.1 M MES-NaOH pH 6.5, 0.5 M NaCl and 2 mM $CaCl_2$) or to the mixture of P1aABD and β4Fn12 (5 µM each prepared in the reaction buffer II consisting of 20 mM HEPES pH 7.5, 50 mM NaCl) and incubated for 30 min at RT. For the two-step cross-linking method, 5 µM CaM or 5 µM β4Fn12 were prepared in the reaction buffer I and II, respectively, and activated with 2 mM EDC and 5 mM sulfo-NHS for 15 min at RT followed by the addition of 20 mM β-mercaptoethanol to quench excessive EDC. Subsequently, P1aABD prepared in the respective reaction buffer was added to the activated protein (CaM or β4Fn12) in equal molar ratio and incubated for 30 min at RT.

Following separation of cross-linking samples by SDS-PAGE and staining of proteins with colloidal Coomassie Blue G-250, protein bands were excised, subjected to in-gel digestion using trypsin and

analyzed by nano-HPLC-ESI-MS/MS using an UltiMate 3000 RSLCnano/LTQ-Orbitrap XL system (Thermo Fisher Scientific, Bremen, Germany) as described (Cristodero et al., 2013). In a first step, data files from LC-MS/MS measurements were analyzed by standard database searches using the programs OMSSA (version 2.1.9) (Geer et al., 2004) and MaxQuant (version 1.3.0.5) (Cox et al., 2011). All searches were done against the amino acid sequences for the recombinant proteins and for a set of common contaminants as provided with the distribution of the MaxQuant program with tryptic specificity allowing up to two missed cleavages. Oxidation of methionine and carbamidomethylation of cysteine residues were considered as variable and fixed modification, respectively. The mass tolerance for precursor ions was set to 5 ppm and for fragment ions to 0.5 Da. Match between runs was applied with a tolerance in retention time of 2 min. In a second step, data were subjected to a stringent search for the identification of cross-linked peptides using in-house developed programs. For this purpose, theoretical tryptic peptides of the recombinant proteins were computed with accurate masses and stored as an indexed table in a MySQL database. For each theoretical peptide, the difference between its accurate mass and the precursor mass of each MS/MS spectrum was computed and queried against the list of peptides indexed by mass using the same mass tolerances as in the first search. The cross-linker specificity was taken into account by retrieving only peptide pairs containing at least one suitable residue on each peptide.

For those peptide pairs matching an accurate precursor mass, the list of theoretical fragment ions was generated and compared to the experimental list of fragment ions. P-values were assigned using the formula used for the Andromeda score (Cox et al., 2011) with minor changes as specified in the following. Neutral losses were considered for the precursor mass but not for fragment masses. Charges of fragment ions were allowed from +1 up to the charge of the precursor minus 1, but only if the charge state was within a tolerance of +/- 1 of the expected charge state based on the number of charged groups in the respective fragment. The expected charge state of fragment ions was computed as the number of basic sites estimated according to a simple scheme (Arg, Lys, N-term: 1; His: 0.5) (Schlosser et al., 2007). $P_{\alpha/\beta}$-values were determined analogously to the calculation of the overall P-value of a cross-linked peptide spectrum match. These values represent the probability of finding at least the number of matched out of the number of theoretical fragment masses by chance for the α-/β-peptide of the cross-linked pair carrying the mass of the complementary peptide at one linkage residue. From the resulting

list of candidate peptide pairs, only those with $P_{\alpha/\beta}$-values below 0.05 were considered as cross-linked peptide spectrum matches.

Quantitative analysis of peptide spectrum matches was performed based on the intensities of peptide features in the allPeptides.txt result file from the MaxQuant program. For this purpose, the text file was stored in a MySQL table. For each peptide spectrum match, the sum of intensities was retrieved for features within the given precursor *m/z*-tolerance and +/- 1 min around the retention time at which the MS/MS spectrum was recorded.

Förster Resonance Energy Transfer (FRET) Experiments

Rat bladder carcinoma 804G cells were grown in Dulbecco's Modified Eagle's Medium (DMEM; Sigma Aldrich) medium, supplemented with 10% heat-inactivated fetal bovine serum and 1% penicillin/streptomycin (both PAA Laboratories). Cells were cultured at 37°C in 5% CO_2 and passaged every third day. Transient transfections of 804G cells were carried out in serum-free media using X-tremeGENE HP (Roche) according to the manufacturer's instructions with 2 µg plasmid and a 1:3 (w/v) ratio of DNA to transfection reagent. Cells were incubated with the transfection complexes for 24 hours and fixed in 4% paraformaldehyde/PIPES (Sigma Aldrich) for additional 24 h. After rinsing with Mg-PBS (phosphate-buffered saline supplemented with 10 mM Mg^{2+}) and water, cells were embedded in glycerol containing 1,4-diazabicyclo[2.2.2]octane (DABCO). FRET was measured by the acceptor photobleaching method as previously described (Stanek and Neugebauer, 2004) using the Leica SP5 confocal microscope. Intensities of CFP (excited by 405 nm laser set to 5–10% of maximum power) and YFP (excited by 514 nm laser line set to 2% of maximum power) were measured. Following this, YFP was bleached in a region of interest by three to five intensive (30% maximum power) pulses of 514 nm laser line and CFP and YFP fluorescence measured again. Apparent FRET efficiency was calculated according to the equation:

$$FRET_{efficiency}\ (\%) = (CFP_{after} - CFP_{before}) \times 100/CFP_{after}$$

Unbleached regions of the same cell were used as a negative control. Only cells displaying similar YFP and CFP signals were measured and cells not matching this criterion were omitted from the analysis. FRET efficiency is given throughout the text as mean ± SEM.

Supplementary Tables

Supplementary Table 1. (Supporting Figure 2)

Zero-length cross-link sites identified for complexes of P1aABD with CaM or integrin β4

Mass / Da	Peptide of P1aABD			Cross-linked peptide						Sum of Intensity
	Sequence [a]	Site	P-value [b]	Construct	Sequence [a]	Site	P-value [b]	P-value [c]	No. of spectra [d]	
1955.9565	ASEGKKDER	K36	6.7E-03	CaM	EAFSLFDK	E15	8.4E-14	4.7E-15	2	8.4 E6
2372.1453	KDER	K37	1.3E-03	CaM	EAFSLFDKDGDGTITTK	E15	7.9E-11	8.4E-14	1	2.1E6
2643.2760	KDERDR	K37	1.6E-03	CaM	EAFSLFDKDGDGTITTK	E15	7.4E-08	5.2E-12	3	8.4E6
1555.7858	ASEGKK	K36	1.9E-03	CaM	EAFSLFDK	E15	1.9E-07	2.0E-11	1	3.0E6
2844.3763	ASEGKKDER	K36	2.8E-02	CaM	EAFSLFDKDGDGTITTK	E15	7.7E-16	1.5E-17	2	7.8E7
1818.8752	EKGR	K92	2.1E-02	CaM	LTDEEVDEMIR	E121	3.2E-12	7.2E-14	1	2.3E6
1818.8766	EKGR	K92	1.5E-02	CaM	LTDEEVDEMIR	E124	1.0E-09	1.3E-11	1	1.8E6
2211.1308	HLIKAQR	K58	1.1E-04	CaM	LTDEEVDEM*IR	E124	2.8E-05	2.9E-10	2	6.6E6
1320.6529	KDERDR	K37	1.0E-03	CaM	EAFR	E88	3.7E-02	2.5E-06	1	1.5E5
1049.5253	KDER	K37	2.5E-02	CaM	EAFR	E88	3.0E-03	2.4E-05	1	8.3E4
1521.7516	ASEGKKDER	K36	1.3E-04	CaM	EAFR	E88	1.9E-02	5.8E-06	2	1.9E6
1513.7656	EKGR	K92	2.1E-02	CaM	HVM*TNLGEK	E115	3.5E-03	6.0E-05	2	1.1E6
1815.9627	KDERDR	K37	1.9E-03	β4Fn12	M*LLIENLR	E161	3.0E-09	2.5E-12	2	9.1E6
1544.8339	KDER	K37	5.9E-04	β4Fn12	M*LLIENLR	E161	4.0E-08	3.6E-11	4	9.3E6
1616.8907	ASEGKK	K36	2.2E-04	β4Fn12	M*LLIENLR	E161	5.4E-07	1.3E-11	2	1.0E7
2001.0679	ASEGKKDER	K36	1.3E-04	β4Fn12	MLLIENLR	E161	5.4E-07	5.0E-11	4	4.1E7

[a] E, K signify site of cross-linker, M*, oxidized methionine
[b] Subscores per peptide
[c] P-value for cross-linked peptide
[d] MS/MS spectra for ion species differing in charge or oxidation state; mass and P-values represent best match

174 ***Supplementary Table 2. (Supporting Figures 3-5)***

175 **SAXS Data-collection and structural parameters**

Sample	**P1aABD/CaM complex**	**P1aABD/β4Fn12 complex**	**P1aABD**
Data collection parameters			
Instrument	SAXS beamline X33 (DESY)	SWING beamline at the synchrotron SOLEIL	SAXS beamline X33 (DESY)
Sample to detector distance (m)	2.7 m	1.8 m	2.7 m
Wavelength (Å)	1.5	1.03	1.5
S range ($Å^{-1}$)	0.08-0.6	0.04-0.38	0.08-0.6
Exposure time (sec)	15	500	15
Temperature (K)	283	283	283
Structural parameters			
I(0) [from *P*(*r*)]	47.44 ± 0.01	0.0429 ± 0.0001	26.05 ± 0.01
R_g (nm) [from *P*(*r*)]	3.17± 0.01	2.90 ± 0.01	2.51 ± 0.01
I(0) (from Guinier)	47.94 ± 0.11	0.0430 ± 0.0057	26.29 ± 0.04
R_g (nm) (from Guinier)	3.17 ± 0.01	2.85 ± 0.6	2.52 ± 0.01
D_{max} (nm)	10.5	9.0	8.8
Porod volume estimate (nm^3)	79.33	55.01	60.91

176 Data are expressed as mean values ± standard deviation.

177

178 ***Supplementary Table 3. (Supporting Results section "Calmodulin Binds to Plectin 1a in an***
179 ***Extended Conformation)***
180
181 **Results of the PBD search for complexes where Ca^{2+}-CaM binds to the interaction partner in**
182 **an extended conformation.**
183
184

PDB	Year of deposition	Name	CaM conformation	Binding *via*
4R8G	2014	Crystal Structure of Myosin-1c tail in complex with Calmodulin	Extended	C-lobe
4BYF	2014	Crystal structure of human Myosin 1c in complex with calmodulin in the pre-power stroke state	Extended	C-lobe
2MGU	2014	Structure of the complex between calmodulin and the binding domain of HIV-1 matrix protein	Extended	Both lobes
4L79	2014	Crystal Structure of nucleotide-free Myosin 1b residues 1-728 with bound Calmodulin	Extended	C-lobe
4DCK	2012	Crystal structure of the C-terminus of voltage-gated sodium channel in complex with FGF13 and CaM	Extended	C-lobe
3SJQ	2012	Crystal structure of a small conductance potassium channel splice variant complexed with calcium-calmodulin	Extended	Both lobes

185
186
187

188 ***Supplementary Table 4. (Supporting Results section "Molecular Determinants of Integrin β4***

189 ***Displacement from the Complex with Plectin 1a by Calmodulin)***

190 **PISA binding interface analyses (Krissinel and Henrick, 2007)**

	$P1aABD_{\Delta22}/CaM_{NL}$		**$P1aABD_{\Delta22}/CaM_{CL}$**		**$P1aABD_{\Delta22}$/β4Fn12**	
	$P1aABD_{\Delta22}$	**CaM_{NL}**	**$P1aABD_{\Delta22}$**	**CaM_{CL}**	**$P1aABD_{\Delta22}$**	**β4Fn12**
Number of atoms	56 (2.8 %)	61 (12.3 %)	57 (2.9 %)	70 (13.3 %)	82 (4.4 %)	75 (5.0 %)
Number of residues	15 (6.2 %)	19 (29.2 %)	15 (6.2%)	23 (35.4 %)	21 (9.3 %)	24 (12.4 %)
Solvent-accessible area ($Å^2$)	665 (5.2 %)	635 (14.9 %)	671 (5.3%)	617 (13.4 %)	700 (5.9 %)	700 (6.3 %)
Solvation energy gain (kcal/mol)	-6.2 (2.9 %)	-6.7 (14.7 %)	-5.2 (2.4 %)	-5.4 (11.2 %)	0.7 (-0.4 %)	-0.1 (0.1 %)
P-value	0.006	0.140	0.021	0.075	0.527	0.591

191

192

Supplementary Figures

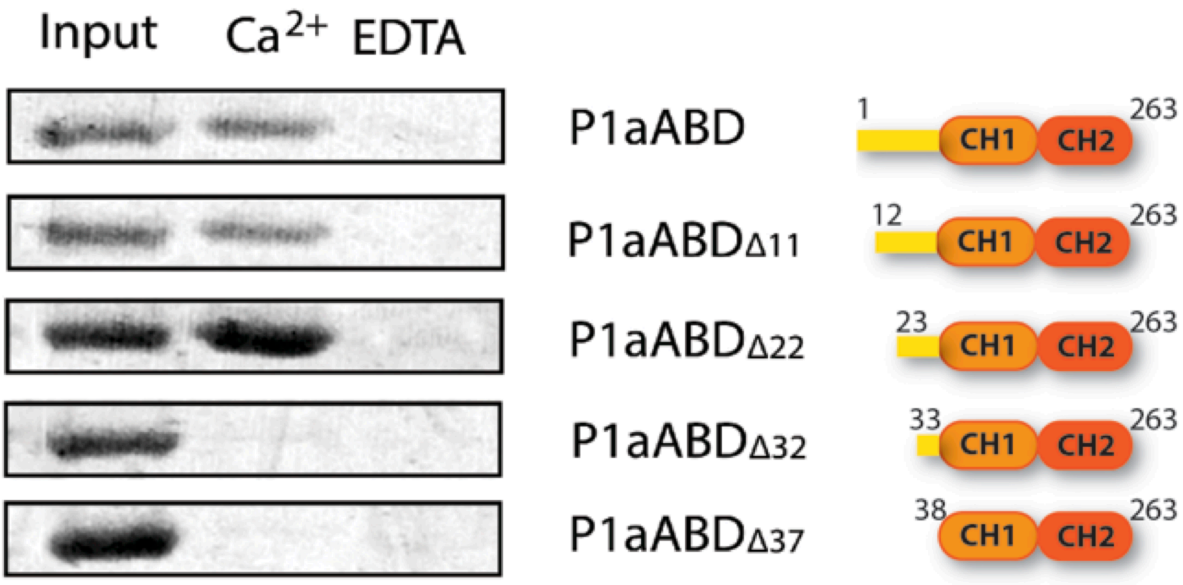

Supplementary Figure 1. (Supporting Results section "Plectin 1a Interacts with the N-ter Lobe of Calmodulin")

Pull-down assay was carried out using CaM-Sepharose beads in the presence of either calcium or EDTA. P1aABD$_{\Delta 22}$, the shortest plectin fragment displaying Ca^{2+}-dependent binding to CaM-Sepharose, was selected for the crystallization trials. Schematic representations show fragments used in the assay.

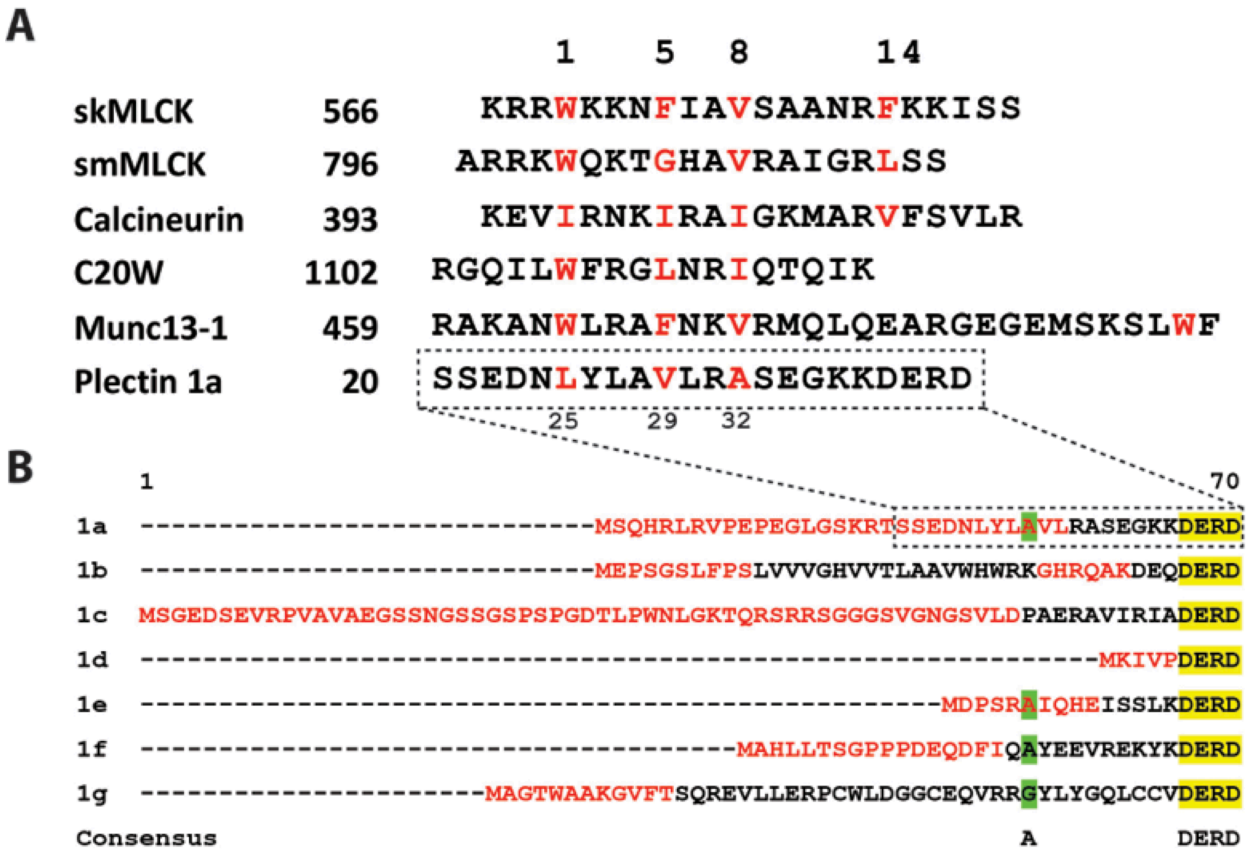

Supplementary Figure 2. (Supporting Results sections "Crystal Structure of the Plectin 1a ABD in Complex with Calmodulin N-ter Lobe" and "Calmodulin Binds to Plectin 1a in an Extended Conformation")

(A) Sequence alignment of CaM binding motifs. The hydrophobic residues corresponding to the CaM binding motifs are highlighted in red. skMLCK, smMLCK, and calcineurin are classified into a 1-5-8-14 motif, whereas C20W and plectin 1a belong to a 1-5-8 motif. Munc13-1 has a 1-5-8-26 CaM-binding motif. (B) The sequence alignment of plectin isoforms. The N-terminal specific sequences of seven isoforms were aligned, showing no sequence similarity among isoforms; conserved residues are shaded in green and identical residues are lightened in yellow. In addition, disordered residues predicted by PrDOS are shown in red.

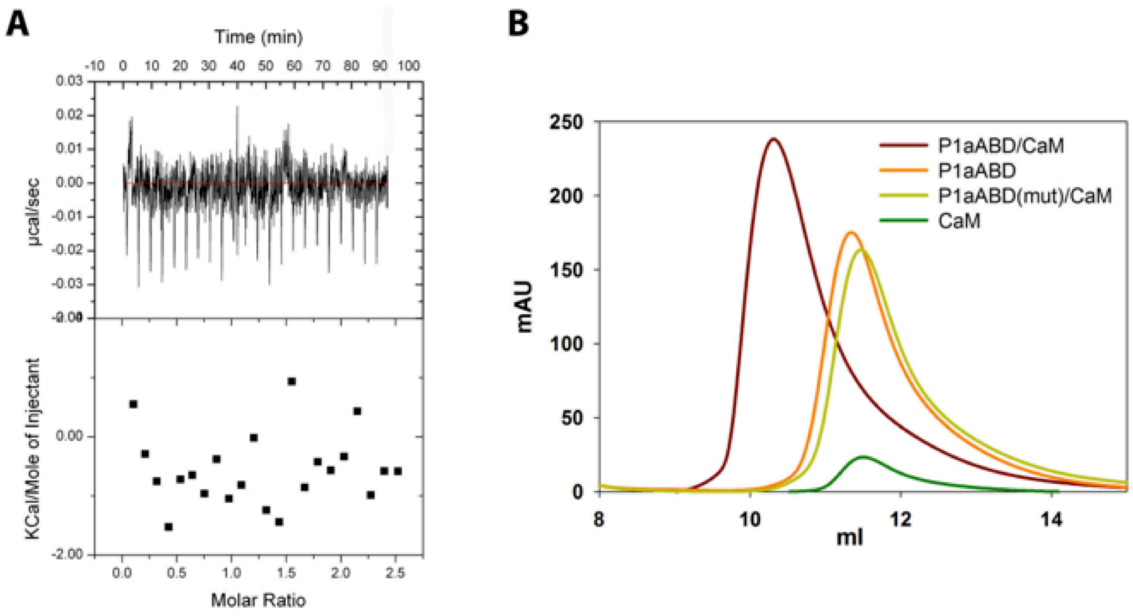

215

216 ***Supplementary Figure 3. (Supporting Results section "Crystal Structure of the Plectin 1a ABD***

217 ***in Complex with Calmodulin N-ter Lobe" and Figure 2)***

218 *In vitro* mutational analyses. **(A)** ITC experiment was carried out to measure the mutational

219 effect on the interaction. CaM is titrated to the P1aABD mutant (Leu25Asp and Val29Asp); no

220 interaction is observed. **(B)** Gel-filtration analyses. When P1aABD is mixed with CaM, it is eluted

221 earlier than CaM and P1aABD, suggesting the complex formation in solution. However P1aABD

222 mutant is not able to associate with CaM.

223

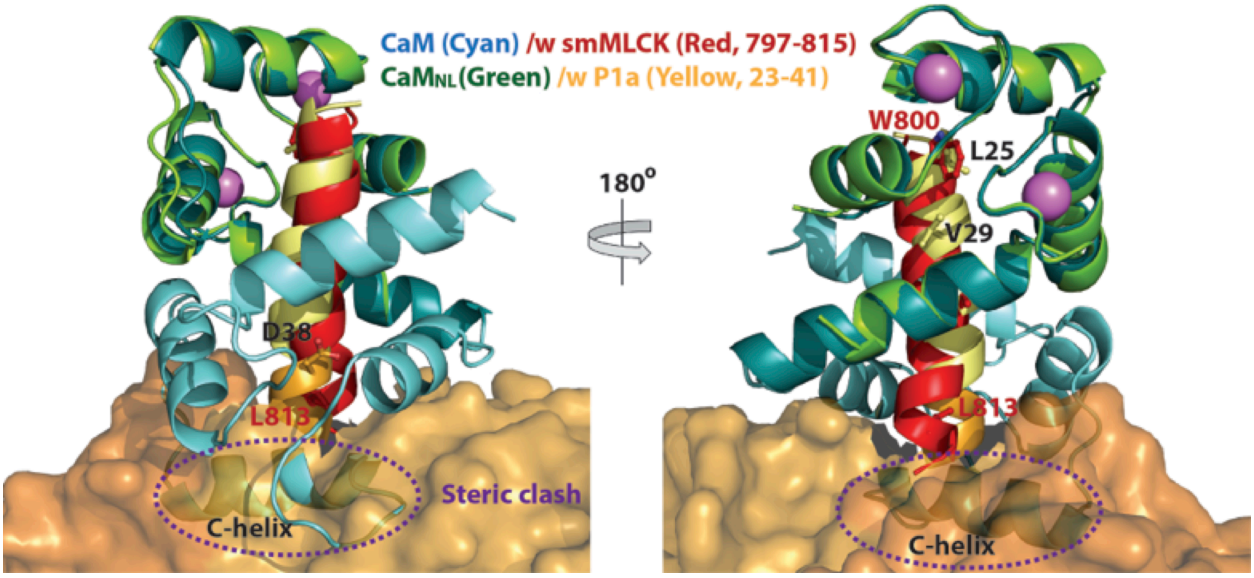

Supplementary Figure 4. (Supporting Results section "Calmodulin Binds to Plectin 1a in an Extended Conformation" and Figure 4)

The crystal structure of the P1aABD$_{\Delta 22}$/CaM$_{NL}$ complex superimposed on the crystal structure of the CaM/smMLCK complex (PDB:1CDL) (RMSD: 0.684Å over 57 Cα); N and C-lobes are respectively displayed in light and dark cyan and smMLCK peptide (797-815 residues) is shown in red. The superposition shows that C-helix of N-lobe makes a steric clash with plectin ABD (shown in an bronze (CH1) and orange (CH2) molecular surface).

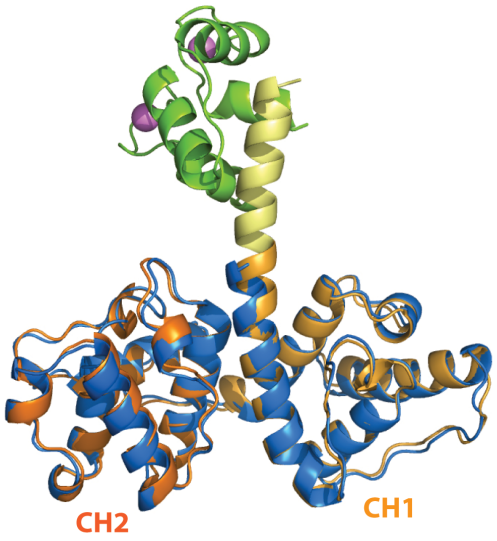

Supplementary Figure 5. (Supporting Results section "Plectin 1a N-terminal Tail Folds upon Binding to Calmodulin" and Figure 4)

The crystal structure of P1aABD$_{\Delta 22}$ is shown in blue and superimposed to the P1aABD$_{\Delta 22}$/CaM$_{NL}$ complex (RMSD: 0.69 Å over 209 equivalent Cα atoms), demonstrating that the Ca^{2+}/CaM binding does not affect the conformation of plectin ABD.

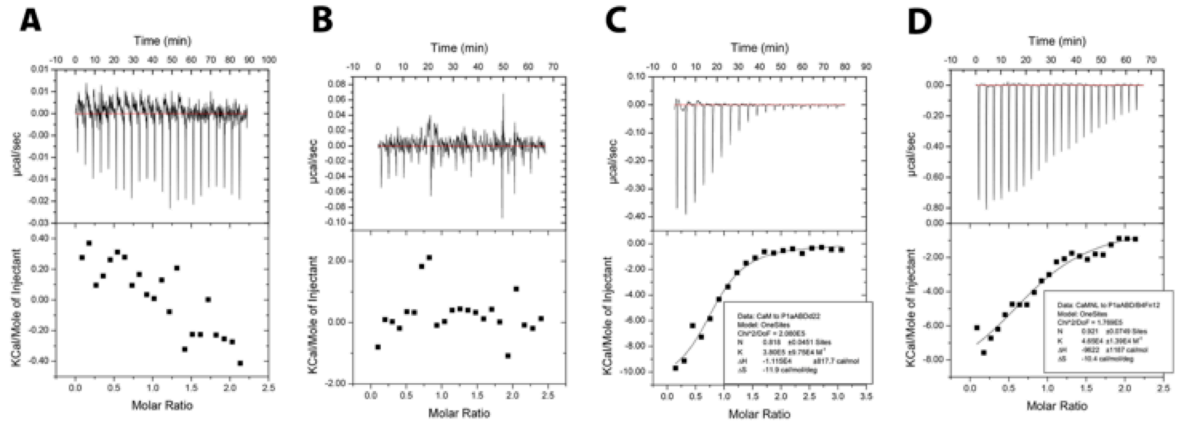

Supplementary Figure 6. (Supporting Results section "N-terminal Tail of Plectin 1a is not Involved in Interaction with Integrin β4" and Figure 7)

ITC analyses **(A)** β4Fn12 (0.04 mM) was titrated with peptide comprising the first 60 N-terminal residues of P1a (0.4 mM) at 30°C, displaying the no interaction. **(B)** β4Fn12 (0.04 mM) was titrated with CaM (0.4 mM) at 30°C, displaying the no interaction. **(C)** P1aABD$_{\Delta 22}$ (0.02mM) was titrated with CaM (0.3 mM); ITC experiment was carried out at 25 °C. The binding affinity of P1aABD$_{\Delta 22}$ to CaM (K_d: 2.6 ± 1.0 µM) is similar to that of P1aABD. **(D)** P1aABD/β4Fn12 complex (0.07 mM) was titrated with CaM$_{NL}$ (0.7 mM); ITC experiment was carried out at 30 °C. CaM$_{NL}$ bound to P1aABD in the presence of β4Fn12 with lower affinity (K_d: 21.5 ± 7.2 µM).

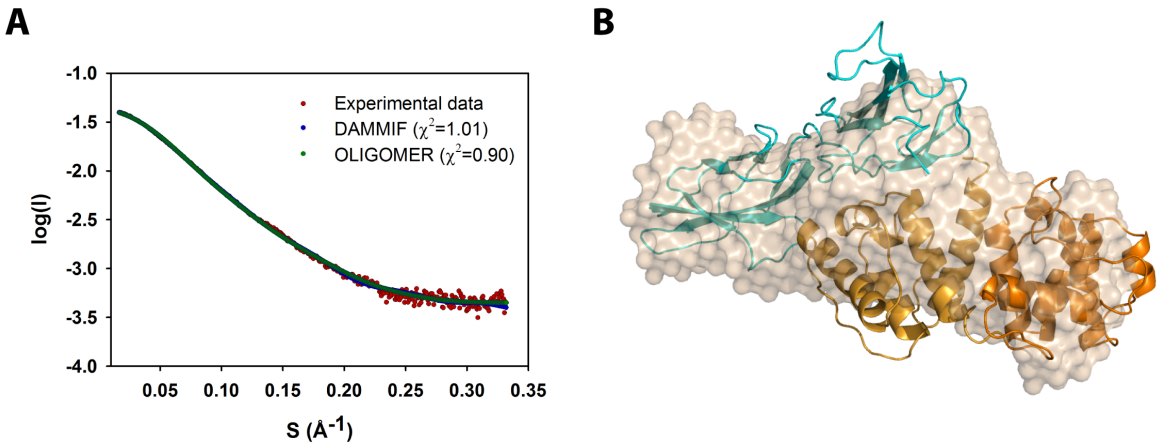

Supplementary Figure 7. (Supporting Results section "N-terminal Tail of Plectin 1a is not Involved in Interaction with Integrin β4" and Figure 6)

(A) SAXS curves. The experimental scattering curve of the P1ABD/β4Fn12 complex is shown in red. An *ab initio* model was fitted to experimental data and is shown in blue. The scattering profile of the crystal structure of the P1aABD$_{\Delta 22}$/β4Fn12 complex supplemented with missing residues was calculated using OLIGOMER and is displayed in green. **(B)** The crystal structure of the P1aABD$_{\Delta 22}$/β4Fn12 complex superimposed on the *ab initio* shell reconstructed from SAXS data .

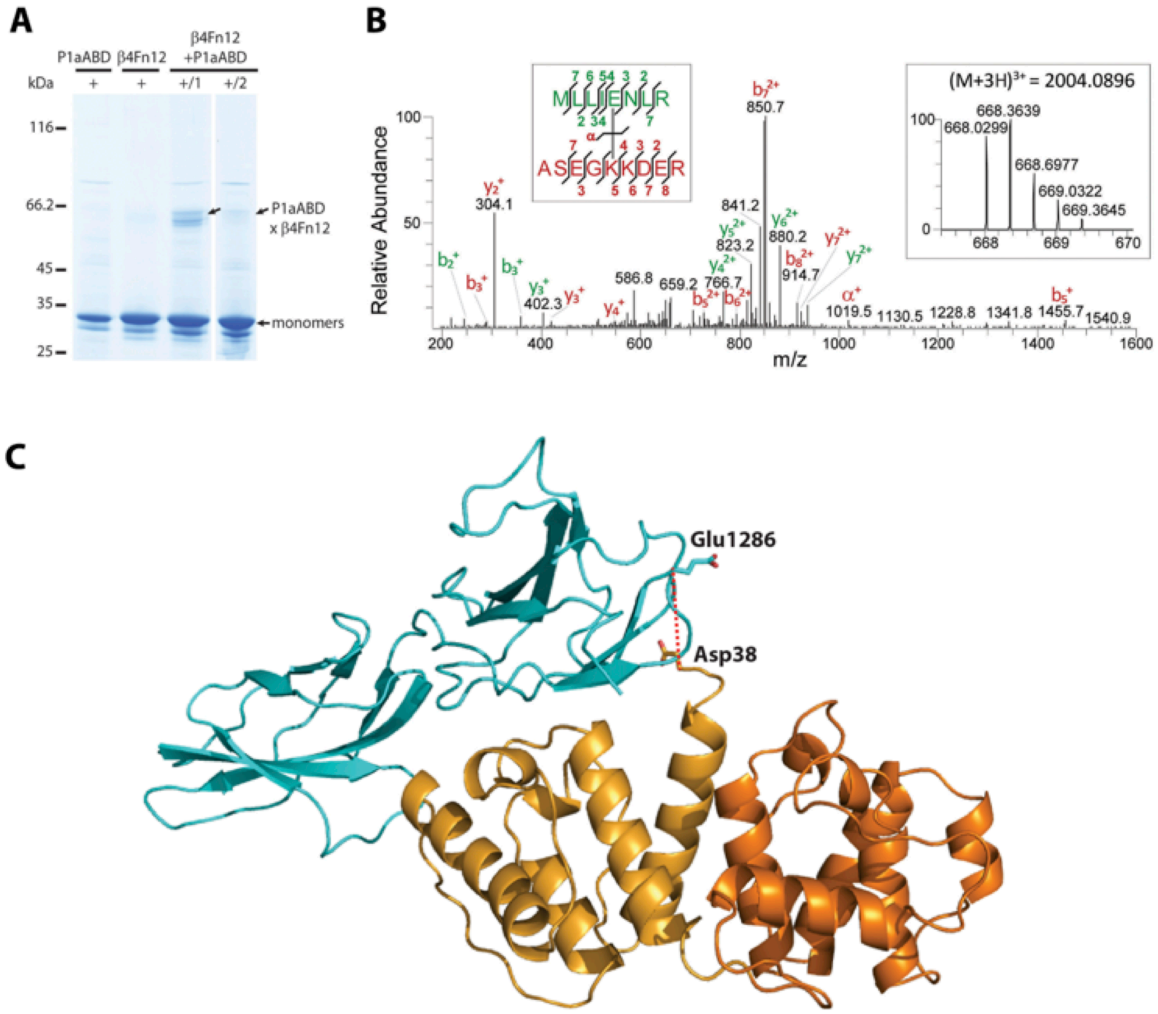

260

261 ***Supplementary Figure 8. (Supporting Results section "N-terminal Tail of Plectin 1a is not***

262 ***Involved in Interaction with Integrin β4" and Figure 6)***

263 **(A)** SDS-PAGE analysis of β4Fn12/P1ABD complex cross-linked by zero-length chemical cross-

264 linker EDC and sulfo-NHS. Proteins were incubated separately with cross-linker (+), in a one-

265 step (+/1) or in a two-step (+/2) reaction activating β4Fn12. **(B)** MS/MS-Spectrum identifying a

266 pair of cross-linked peptides after in-gel proteolysis of the P1ABD/β4Fn12 complex. **(C)** Crystal

267 structure of the P1aABD/β4Fn12 shows that the cross-linking and MS results are consistent

268 with the crystal structure. A distance between two Cα atoms (integrin β4 Glu1286 and plectin

269 Asp38) is 12.97 Å.

270

A

```
N-lobe   9    IAEFKEAFSLFDKDGDGTITTKELGTVMRSLGQ  41
C-lobe   82   EEEIREAFRVFDKDGNGYISAAELRHVMTNLGE  114
         42   NPTEAELQDMINEVDADGNGTIDFPEFLTMMA   73
         115  KLTDEEVDEMIREADIDGDGQVNYEEFVQMMT   146
```

B

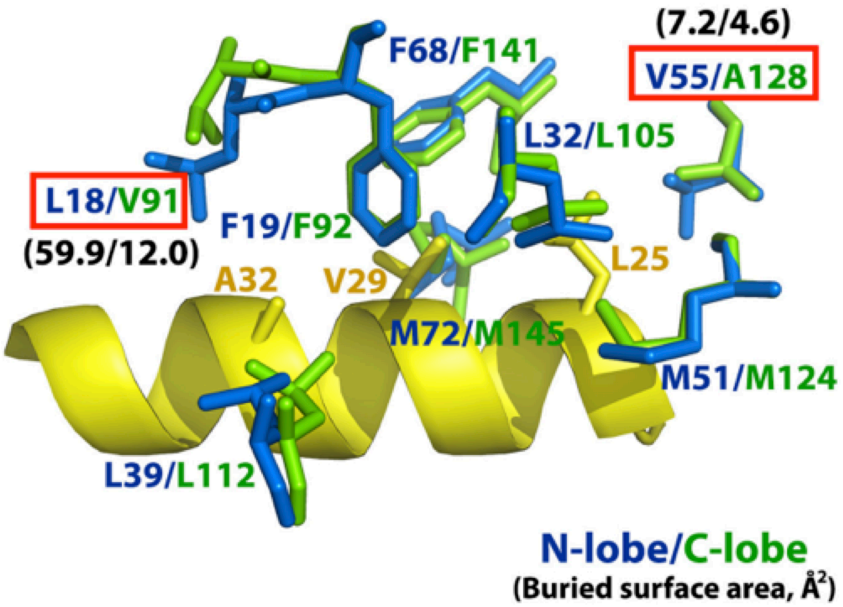

271

272 ***Supplementary Figure 9. (Supporting Results section "Molecular Determinants of Integrin β4***
273 ***Displacement from the Complex with Plectin 1a by Calmodulin")***

274 **(A)** The sequence alignment of each lobe of CaM. The interfacing residues were analyzed by
275 PDBePISA and shaded in yellow. Different residues between two lobes are shown in red **(B)**
276 Interfacing hydrophobic residues of two lobes determined by Ligplot are superimposed and
277 shown in sticks; N-lobe in blue and C-lobe in green, showing that Leu18 (59.9 $Å^2$) and Val55 (7.2
278 $Å^2$) in N-lobe offer a larger surface areas than Val91 (12.0 $Å^2$) and Ala128 (4.6 $Å^2$) in C-lobe.
279 Hydrophobic residues of P1a corresponding to a 1-5-8 motif (Leu25-Val29-Ala32) are displayed
280 in yellow.

References

Babu, Y.S., Bugg, C.E., and Cook, W.J. (1988). Structure of calmodulin refined at 2.2 A resolution. J Mol Biol *204*, 191-204.

Bernado, P., Mylonas, E., Petoukhov, M.V., Blackledge, M., and Svergun, D.I. (2007). Structural characterization of flexible proteins using small-angle X-ray scattering. J Am Chem Soc *129*, 5656-5664.

Blanchet, C.E., Zozulya, A.V., Kikhney, A.G., Franke, D., Konarev, P.V., Shang, W.F., Klaering, R., Robrahn, B., Hermes, C., Cipriani, F*., et al.* (2012). Instrumental setup for high-throughput small- and wide-angle solution scattering at the X33 beamline of EMBL Hamburg. J Appl Crystallogr *45*, 489-495.

Cox, J., Neuhauser, N., Michalski, A., Scheltema, R.A., Olsen, J.V., and Mann, M. (2011). Andromeda: a peptide search engine integrated into the MaxQuant environment. J Proteome Res *10*, 1794-1805.

Cristodero, M., Mani, J., Oeljeklaus, S., Aeberhard, L., Hashimi, H., Ramrath, D.J., Lukes, J., Warscheid, B., and Schneider, A. (2013). Mitochondrial translation factors of Trypanosoma brucei: Elongation factor-Tu has a unique subdomain that is essential for its function. Mol Microbiol.

David, G., and Perez, J. (2009). Combined sampler robot and high-performance liquid chromatography: a fully automated system for biological small-angle X-ray scattering experiments at the Synchrotron SOLEIL SWING beamline. J Appl Crystallogr *42*, 892-900.

Franke, D., and Svergun, D.I. (2009). DAMMIF, a program for rapid ab-initio shape determination in small-angle scattering. J Appl Crystallogr *42*, 342-346.

Geer, L.Y., Markey, S.P., Kowalak, J.A., Wagner, L., Xu, M., Maynard, D.M., Yang, X., Shi, W., and Bryant, S.H. (2004). Open mass spectrometry search algorithm. J Proteome Res *3*, 958-964.

Konarev, P.V., Volkov, V.V., Sokolova, A.V., Koch, M.H.J., and Svergun, D.I. (2003). PRIMUS: a Windows PC-based system for small-angle scattering data analysis. J Appl Crystallogr *36*, 1277-1282.

Kostan, J., Gregor, M., Walko, G., and Wiche, G. (2009). Plectin isoform-dependent regulation of keratin-integrin alpha6beta4 anchorage via Ca2+/calmodulin. The Journal of biological chemistry *284*, 18525-18536.

Krissinel, E., and Henrick, K. (2007). Inference of macromolecular assemblies from crystalline state. J Mol Biol *372*, 774-797.

Niessen, C.M., Hulsman, E.H., Oomen, L.C., Kuikman, I., and Sonnenberg, A. (1997). A minimal region on the integrin beta4 subunit that is critical to its localization in hemidesmosomes regulates the distribution of HD1/plectin in COS-7 cells. J Cell Sci *110 (Pt 15)*, 1705-1716.

Petoukhov, M.V., Franke, D., Shkumatov, A.V., Tria, G., Kikhney, A.G., Gajda, M., Gorba, C., Mertens, H.D.T., Konarev, P.V., and Svergun, D.I. (2012). New developments in the ATSAS program package for small-angle scattering data analysis. J Appl Crystallogr *45*, 342-350.

Rezniczek, G.A., de Pereda, J.M., Reipert, S., and Wiche, G. (1998). Linking integrin alpha6beta4-based cell adhesion to the intermediate filament cytoskeleton: direct interaction between the beta4 subunit and plectin at multiple molecular sites. J Cell Biol *141*, 209-225.

Schlosser, A., Vanselow, J.T., and Kramer, A. (2007). Comprehensive phosphorylation site analysis of individual phosphoproteins applying scoring schemes for MS/MS data. Anal Chem *79*, 7439-7449.

Stanek, D., and Neugebauer, K.M. (2004). Detection of snRNP assembly intermediates in Cajal bodies by fluorescence resonance energy transfer. J Cell Biol *166*, 1015-1025.

Svergun, D. (1992). Determination of the regularization parameter in indirect-transform methods using perceptual criteria. J Appl Crystallogr *25*, 495-503.

Volkov, V.V., and Svergun, D.I. (2003). Uniqueness of ab initio shape determination in small-angle scattering. J Appl Crystallogr *36*, 860-864.